PHILOSOPHICAL TRANSACTIONS OF THE ROYAL SOCIETY A MATHEMATICAL, PHYSICAL & ENGINEERING SCIENCES

Head-On Collision of Normal Shock Waves with a Rubber-Supported Wall

G. Mazor, O. Igra, G. Ben-Dor, M. Mond and H. Reichenbach

Phil. Trans. R. Soc. Lond. A 1992 **338**, 237-269
doi: 10.1098/rsta.1992.0008

Head-on collision of normal shock waves with a rubber-supported wall

By G. Mazor[1], O. Igra[1], G. Ben-Dor[1], M. Mond[1] and H. Reichenbach[2]

[1] *The Pearlstone Center for Aeronautical Engineering Studies, Department of Mechanical Engineering, Ben-Gurion University of the Negev, Beer Sheva 84105, Israel*

[2] *Ernst Mach Institute, Freiburg D-7800, F.R.G.*

Contents

The head-on collision between a normal shock wave, propagating into a quiescent gas, and a rubber-supported plate was investigated theoretically and experimentally. In the theoretical part, a physical model was developed for describing the collision process. Three different modes in which the rubber could be loaded, due to its collision with the incident shock wave, were studied. They are: uni-axial stress loading, bi-axial stress loading and uni-axial strain loading. In the first two modes the rubber can expand while carrying the shock-wave induced compressive load, and therefore can be treated as an incompressible medium. This is not the case in a uni-axial strain loading where the rubber cannot expand while carrying the shock-wave-induced load. The model developed was based on both the conservation equations and on an appropriate strain–stress relation which describes the rubber behaviour under loading. The model was solved numerically for each of the above-mentioned loading modes. Experiments were conducted in a shock tube; the rubber response to its collision with normal shock wave was studied for the case of bi-axial stress loading. Pressures, in the gas, and stresses, in the rubber, were recorded by using piezoelectric pressure transducers; the shock-wave reflection, in the gas, and the rubber displacement and compression processes were recorded on successive shadowgraphs. Good agreement was found between the experimental and numerical results for the case of bi-axial stress loading. This agreement validates the model developed for the collision process and the reliability of the numerical scheme used for its solution.

Phil. Trans. R. Soc. Lond. A (1992) **338**, 237–269
Printed in Great Britain

1. Introduction

Head-on reflection of normal shock waves from rigid boundaries is well known and documented (Courant & Friedrichs 1948; Glass & Hall 1959). In such cases, the head-on reflection phenomena is characterized by a zero flow velocity behind the reflected shock wave. In nature, however, head-on reflection of normal shock waves from non-rigid boundaries can occur. Cases in which one finds shock wave reflection from, and propagation into, a non-rigid medium appear in many engineering problems. Some typical examples are: reflection of blast waves from rubber-coated bodies that can be found on a battle ground; shock-wave reflection from, and penetration into, live-tissue such as in the case of litotherapy (shattering kidney and bladder stones by the focusing of weak shock waves), and the interaction of shock waves with foams used for pressure amplifications. It is therefore of interest to better understand the head-on collision of normal shock waves with such boundaries. Alpher & Rubin (1954), Meyer (1957) and Wlodarczyk (1980) extended the solution of shock-wave reflection to the case of a head-on collision with a rigid boundary which is free to move. In such a case, due to the pressure difference acting on the rigid wall, it accelerates in the direction of the incident shock wave, and thereby transmits compression waves ahead of it and expansion waves behind it. The compression waves will coalesce to a shock wave while the expansion waves will overtake the reflected shock wave and weaken it. This process continues until the pressure difference across the rigid wall diminishes. At that time the shock wave produced by the moving wall and the wall attain constant velocities, while the reflected shock wave is reduced to a Mach wave.

Beavers & Matta (1972) and Clarke (1984) studied the head-on reflection of weak shock waves from rigid, porous materials. The aim of their work was to study how porosity affects the strength of the reflecting shock wave. In their work it was assumed that the porous material is dense enough to prevent transmission of an incident shock wave through it, and that the reflected shock wave propagates at a constant velocity. Under this assumption they developed an analytical model which described the shock-wave reflection and the flow field through the porous material.

A few authors studied the head-on reflection of normal shock waves from solid flexible boundaries. In these studies the reflecting boundary experienced a deformation as a result of its head-on collision with the normal shock wave. Now the boundary's material elasticity is not ignored, as was the case in the previously cited studies. The following cases of normal shock wave head-on reflection from solid, flexible boundaries were studied.

1. Shock-wave reflection from a steady, solid, linearly elastic boundary (Pack 1957).

2. Shock-wave reflection from various solid, sponge-like materials (Muirhead 1958).

3. Shock-wave reflection from a stationary, solid wall which experiences some deformation (Monti 1970).

4. Shock-wave attenuation in a stationary, flexible material (Wienfield & Hill 1977; Borisov *et al.* 1978).

5. Shock-wave reflection from a stationary, flexible porous foam (Gelfand *et al.* 1983).

6. Shock-wave reflection from a rigid wall, supported by a dumping system that can experience deformation (Wlodarczyk 1981).

A critical review of the above-cited references can be found in Mazor (1989).

However, to the best of our knowledge, the more realistic and complicated case of head-on reflection from nonlinear elastic boundaries, which can experience large deformation, has not been treated as yet. It is the purpose of the present paper to solve the entire flow field which results from a head-on collision of a normal shock wave with a nonlinear elastic medium, for example rubber. Such a material can experience large deformations in its elastic region. Thus, the waves system, which results from the collision, as well as the flow properties behind these waves are investigated both numerically and experimentally.

2. Theoretical background

The problem to be solved is shown schematically in figure 1. A normal shock wave propagates in the gas from left to right at a constant velocity, V_s. At time $t = 0$ the shock wave collides, head-on, with a rigid plate, d (whose mass is w_d), which is supported by a rubber rod (having an initial length L_{r0} and an initial cross-sectional area A_{r0}). Following the collision, depending on the boundary conditions imposed on the rubber rod, one of the following three loading modes are possible.

1. *Uni-axial stress*. The rubber rod's movement is limited only at its rear end, along the x-axis, where it is attached to a rigid boundary. The rubber is free to expand along the y- and z-axis, and its leading edge is free to move along the x-axis (see figure 1*a*). In this case $\sigma_y = \sigma_z = 0$ and $\epsilon_y = \epsilon_z \neq 0$.

2. *Bi-axial stress*. The rubber rod's movements are limited at its rear end, along the x-axis, as well as along the y-axis. (Due to its attachment to rigid boundaries at these locations, see figure 1*b*). The rubber is free to expand along the z-axis and its leading edge can move along the x-axis. In this case $\sigma_z = 0$ and $\epsilon_y = 0$.

3. *Uni-axial strain*. The rubber movements along the y- and z-axis and at its rear end are limited by rigid walls (see figure 1*c*). Only the rubber's leading edge can move along the x-axis. In this case $\epsilon_y = \epsilon_z = 0$ and σ_x, σ_y and $\sigma_z \neq 0$.

In the following, the conservation equations governing the flow field developed in the gaseous phase and the rubber motion are outlined using the lagrangian approach. In developing these equations for the gaseous phase it is assumed that (*a*) the flow is one-dimensional and the gas is an ideal fluid, i.e. inviscid ($\mu = 0$) and thermally non-conductive ($k = 0$); (*b*) the gas can be treated as a perfect gas, i.e. its equation of state is $P = \rho RT$ and its internal energy is given by $e = C_v T$ where P, ρ and T are the gas pressure, density and temperature, respectively; C_v is its specific heat capacity at constant volume, and R is the gas constant. This assumption is reasonable for the moderate shock wave Mach numbers used in the present study; $1 \leqslant M_s \leqslant 4$. (*c*) All body forces can be ignored.

In the lagrangian approach every mass element is identified by a number h which marks its position in the xt-plane. Generally h is chosen to identify the mass element location at some reference time, say at $t = 0$. In the present study it is convenient to identify h on the basis of mass conservation. Consider a flow through a duct having a constant cross-section area, A. The flow is along the duct axis which coincides with the x-axis. Assigning the value $h = 0$ to some reference section in the duct (which moves with the flow), then h expresses the mass contained in the duct between section h and the reference section, i.e.

$$h = \int_{x(0,t)}^{x(h,t)} \rho A \, \mathrm{d}x,$$

where ρ is the density at location x at time t.

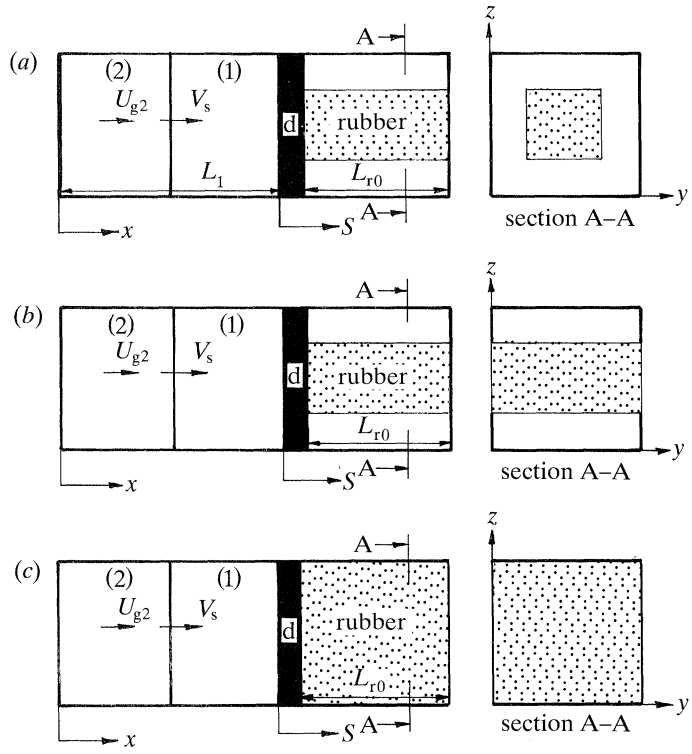

Figure 1. Schematic illustration of three modes for applying a shock-wave-induced compressive load: (*a*) uni-axial stress loading, (*b*) bi-axial stress loading, (*c*) uni-axial strain loading.

The conservation of mass, in the gas flow, is easily obtained by taking the derivative of

$$h_g = \int_{x(0,t)}^{x(h,t)} \rho_g A_g \, dx, \quad \text{i.e.} \quad \rho_g(h_g, t) \frac{\partial x(h_g, t)}{\partial h_g} A_g = 1.$$

Subscript g stands for the gaseous phase. Taking the time derivative of the last expression yields the mass conservation equation, which is

$$\frac{\partial}{\partial t}\left[\rho_g(h_g, t) \frac{\partial x(h_g, t)}{\partial h_g}\right] = 0. \tag{1}$$

The flow velocity U_g is defined as

$$U_g(h_g, t) = \partial x(h_g, t)/\partial t. \tag{2}$$

Using this definition, the conservation of momentum is easily obtained for the considered perfect gas, i.e.

$$\rho_g(h_g, t)\, \partial^2 x(h_g, t)/\partial t^2 = -\partial P(h_g, t)/\partial x. \tag{3}$$

Since

$$\frac{\partial P(h_g, t)}{\partial x} = \frac{\partial P(h_g, t)}{\partial h_g}\frac{\partial h_g}{\partial x}$$

and from,

$$h_g = \int_{x(0,t)}^{x(h,t)} \rho_g A_g \, dx$$

we have $\partial h_g/\partial x = \rho_g(h_g, t) A_g$; therefore, the pressure derivative in (3) could be replaced by

$$\partial P(h_g, t)/\partial x = (\partial P(h_g, t)/\partial h_g)\, \rho_g(h_g, t)\, A_g$$

and (3) can be written as

$$\partial U_g(h_g, t)/\partial t = -A_g \, \partial P(h_g, t)/\partial h_g. \tag{4}$$

The conservation of energy, for the considered gas is

$$\partial e(h_g, t)/\partial t = -P(h_g, t)\, \partial V_g(h_g, t)/\partial t, \tag{5}$$

where e, the internal energy, is given by

$$e(h_g, t) = C_v T(h_g, t)$$

and V_g, the specific volume, is given by $V_g = 1/\rho_g$. From the equation of state we have

$$P(h_g, t) = RT(h_g, t)/V_g(h_g, t). \tag{6}$$

In developing the conservation equations for the rubber we make the following assumptions.

1. The rubber medium is an isotropic elastic body and the changes in its internal energy are negligibly small.

2. Body forces (gravity) and friction forces acting on the external surfaces of the rubber rod are negligibly small. This assumption is perfectly right for the uni-axial stress case. In the other two loading modes its validity depends on the ability to reduce friction between the rubber and the rigid boundaries by using proper lubrication.

3. Stresses developed in the rubber rod are uniformly distributed along any cross-sectional area perpendicular to the x-axis. Therefore, the rubber's cross-sectional area remains planar throughout the deformation process.

4. The rubber rod does not buckle due to the compressive loads imposed on it by the shock wave. The validity of this assumption depends upon the size of the rubber rod and the strength of the colliding shock wave (see Mazor 1989). The conditions chosen in the present study ensured that no buckling could occur.

The lagrangian variable for the rubber medium h_r, is defined as

$$h_r = \int_{s(0,t)}^{s(h_r,t)} \rho_r A_r \, dS, \tag{7}$$

where subscript r stands for the rubber and S is the axial position of area A_r at time t. Following the procedure described earlier the conservation of mass for the rubber is

$$\frac{\partial}{\partial t}\left[\rho_r(h_r, t)\frac{\partial S(h_r, t)}{\partial h_r} A_r(h_r, t)\right] = 0. \tag{8}$$

For defining a particle velocity in the rubber medium let us consider a mass element dm whose position at $t = 0$ was $x = X_0$ and its width was dX_0 (see figure 2).

Figure 2

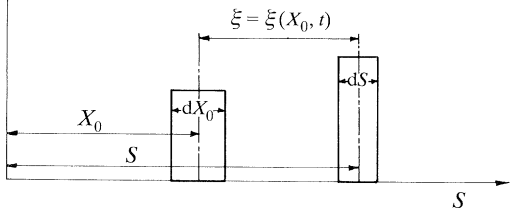

Figure 3

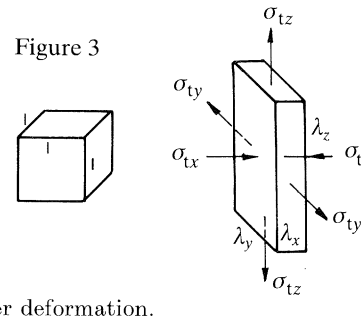

Figure 2. Illustration of a mass element before and after deformation.

Figure 3. Illustration of a cubical element (free of stress) and its deformed geometry while carrying a compressive load along the x-axis.

Due to the rubber deformation it moved to S and its width changed to $\mathrm{d}S$. It is apparent from figure 2 that $S = X_0 + \xi$, where ξ is the magnitude of the displacement along the S-axis. The rubber particle velocity is therefore

$$U_r(h_r, t) = \partial\xi(h_r, t)/\partial t \quad \text{or} \quad U_r(h_r, t) = \partial S(h_r, t)/\partial t. \tag{9}$$

The extension ratio in the x-direction, λ_x (reduction in case of compressive loads), which expresses the ratio between the element's width after and before the deformation is therefore

$$\lambda_x(h_r, t) = \partial S(h_r, t)/\partial X_0. \tag{10}$$

From

$$\frac{\partial S(h_r, t)}{\partial X_0} = \frac{\partial S(h_r, t)}{\partial h_r}\frac{\partial h_r}{\partial X_0}$$

and using the definition of h_r (which can also be expressed as

$$h_r = \int_0^{x_0} \rho_{r0} A_{r0}\, \mathrm{d}X_0)$$

(10) can be rewritten as

$$\lambda_x(h_r, t) = \rho_{r0} A_{r0}\, \partial S(h_r, t)/\partial h_r, \tag{11}$$

where subscript 0 indicates pre-deformation values. For a body under compressive loads $0 < \lambda < 1$, for tensile conditions $\lambda > 1$, and when no load acts on the body (stressless condition) $\lambda = 1$.

For a mass element $\mathrm{d}m$, $\mathrm{d}m = \rho_r\, \mathrm{d}S\, A_r = \rho_{r0}\, \mathrm{d}X_0\, A_{r0}$ (see figure 2) Newton's second law implies

$$\rho_{r0} A_{r0} \frac{\partial U_r}{\partial t}\mathrm{d}X_0 = -\frac{\partial F_x}{\partial S}\mathrm{d}S;$$

in a lagrangian coordinate system this can be expressed as:

$$\frac{\partial}{\partial t}(\mathrm{d}m\, U_r) = -\frac{\partial F_x}{\partial X_0}\mathrm{d}X_0. \tag{12}$$

Substituting the expressions obtained for U_r and $\mathrm{d}m$ yields

$$\rho_{r0} A_{r0}\, \partial^2\xi/\partial t^2 = -\partial F_x/\partial X_0. \tag{13}$$

Equation (13) represents the conservation of momentum for the rubber under deformation.

The 'nominal stress' (sometimes called 'engineering stress') is defined as the ratio between the normal force, acting on a given surface at time t, and the surface area before deformation (i.e. at $t = 0$);

$$\sigma(h_r, t) = F(h_r, t)/A_{r0}. \tag{14}$$

For compressive loads $\sigma < 0$ while under tension $\sigma > 0$. Using the 'nominal stress' definition in (13) and taking the absolute value of σ (i.e. $|\sigma(h_r, t)|$) yields (for both compressive and tension loads):

$$\partial^2\xi(h_r, t)/\partial t^2 = -(1/\rho_{r0})\,\partial|\sigma_x(h_r, t)|/\partial X_0. \tag{15}$$

$|\sigma_x|$ is the absolute value of the nominal stress in the x-direction. Equation (15) is the equation of motion for a rubber element. From (9) $\partial^2\xi(h_r, t)/\partial t^2 = \partial^2 S(h_r, t)/\partial t^2$ and from the definition of h_r we obtain

$$\frac{\partial|\sigma_x(h_r, t)|}{\partial X_0} = \frac{\partial|\sigma_x(h_r, t)|}{\partial h_r}\frac{\partial h_r}{\partial X_0} = \frac{\partial|\sigma_x(h_r, t)|}{\partial h_r}\rho_{r0}A_{r0}.$$

Substituting the last two terms into (15) provides the equation of motion for the rubber element in terms of the lagrangian variable h_r, i.e.

$$\frac{\partial^2 S(h_r, t)}{\partial t^2} = -A_{r0}\frac{\partial|\sigma_x(h_r, t)|}{\partial h_r} \quad \text{or} \quad \frac{\partial U_r(h_r, t)}{\partial t} = -A_{r0}\frac{\partial|\sigma_x(h_r, t)|}{\partial h_r}. \tag{16}$$

Equations (1), (2), (4), (5), (6), (8), (9), (11) and (16) compose a set of nine equations with eleven dependent variables (ρ_g, P, T, U_g, X, ρ_r, σ_x, λ_x, S, A_r and U_r). To make this set solvable two additional equations are needed. The equations formulated so far apply to a compressible solid medium under compressive loads. For rubber under a uni-axial stress, or bi-axial stress, it is perfectly right to assume that the rubber rod is incompressible. (Its volume remains constant during its loading.) For such a case $\rho_r = \rho_{r0}$ and the number of dependence variables is reduced to ten. The additional equation needed for obtaining a closed set of equations is a relation between the rubber stress and its extension ratio.

For describing a perfectly elastic body, relations between the three principal stresses (σ_{tx}, σ_{ty} and σ_{tz}, defined as $\sigma_{ti} = F_i/A_r$) and the appropriate principal extension ratios (λ_x, λ_y and λ_z; see figure 3) are needed. These relations can be expressed in terms of the strain energy function W, which represents the work, per unit volume, associated with the body's deformation. In the following, a correlation proposed for relating σ and λ is briefly presented. This correlation, based upon the statistical theory, agrees well with available experimental data for rubber under compressive loads (Treloar 1974). Other correlations were proposed for relating the stress and strain in rubber. For example, the correlation based on the Valanis–Landel (1967) hypothesis. In Mazor (1989) both the correlation based upon the statistical theory and the one based on the Valanis–Landel hypothesis were used. Since both yielded practically identical results for the computed rubber properties (Mazor 1989), only the statistical theory is briefly presented in the following and shall be used in the numerical solution.

(*a*) *The statistical theory*

For an incompressible rubber the principal stress σ_{ti} is (Treloar 1974)

$$\sigma_{ti} = \lambda_i\partial W/\partial\lambda_i - P, \tag{17}$$

where $i = x, y$ or z and P is an arbitrary hydrostatic pressure. The relation between the principal stress and the nominal stress (14) is,

$$\sigma_i = \sigma_{ti}/\lambda_i \quad (i = x, y, z). \tag{18}$$

From the molecular theory of rubber elasticity, which is based on a statistical mechanics approach to the molecular chains composing the rubber, when there is no change in the rubber's internal energy the following equation describes the strain-energy function W (Treloar 1974). This function W, represents the deformation work, or the elastically stored energy, per unit volume of the material:

$$W = \tfrac{1}{2}G[\lambda_x^2 + \lambda_y^2 + \lambda_z^2 - 3], \tag{19}$$

where $G = NkT$ is a constant determined by the network structure; N is the number of molecular chains per unit volume and k is the Boltzmann's constant. It is apparent from (19) that the deformation work (or strain energy) depends on one physical parameter, G. This parameter expresses the rubber elasticity and is dependent upon N. Combining (17) and (19) yields

$$\sigma_{ti} = G\lambda_i^2 - P \quad (i = x, y, z). \tag{20}$$

The difference between the principal stresses can easily be obtained from (20);

$$\sigma_{tx} - \sigma_{ty} = G[\lambda_x^2 - \lambda_y^2], \quad \sigma_{tx} - \sigma_{tz} = G[\lambda_x^2 - \lambda_z^2]. \tag{21}$$

In the following the strain–stress relations for the three different loading modes, defined earlier, are developed.

(*b*) *Uni-axial stress loading*

In the case shown in figure 1*a*, $\sigma_{tz} = \sigma_{ty} = 0$ and $\lambda_y = \lambda_z$. For an incompressible medium $\lambda_x \lambda_y \lambda_z = 1$ and therefore, $\lambda_y = \lambda_z = \lambda_x^{-\frac{1}{2}}$. For this case, (21) yields $\sigma_{tx} = G[\lambda_x^2 - 1/\lambda_x]$. Together with (18) the nominal stress is given by

$$\sigma_x(h_r, t) = G[\lambda_x(h_r, t) - \lambda_x^{-2}(h_r, t)]. \tag{22}$$

In compression $\lambda_x < 1$ and therefore, $\sigma_x(h_r, t) < 0$. Materials conforming with (22) are called neo-hookean materials. Experiments made by Treloar (1958) verify that (22) accurately describes rubber under compressive loads.

(*c*) *Bi-axial stress loading*

In this case, shown in figure 1*b*, $\lambda_y = 1$. For an incompressible material $\lambda_z = \lambda_x^{-1}$. Substituting these into (18) and (21) yields

$$\sigma_x = G[\lambda_x - \lambda_x^{-3}] + \sigma_z \lambda_x^{-2} \tag{23}$$

when the rubber's lateral inertia could be ignored ($\sigma_z = 0$) one obtains for the nominal stress in the x-direction:

$$\sigma_x(h_r, t) = G[\lambda_x(h_r, t) - \lambda_x^{-3}(h_r, t)], \tag{24}$$

and for the nominal stress in the y-direction:

$$\sigma_y(h_r, t) = G[1 - \lambda_x^{-2}(h_r, t)]. \tag{25}$$

(*d*) *Uni-axial strain loading*

Unlike the uni-axial and bi-axial stress cases, where it is safe to assume that the rubber volume remains constant, in a uni-axial strain case the rubber will experience a small reduction in its volume. Small because the rubber's Poisson ratio is within the

range $0.47 < \nu \leqslant 0.5$; materials having $\nu = 0.5$ do not change their volume under a uni-axial stress condition. It is therefore reasonable to assume that the changes in the rubber volume will be very small for the pressures generated by shock waves in the range $M_s \leqslant 4$. Based on this assumption the stress–strain relation for the case of a uni-axial strain loading is subsequently derived. Since we are dealing with compressive loads only, in the following we adopt the non-standard convention in which strains (ϵ_x, ϵ_y, ϵ_z) are positive in contraction and stresses are positive in compression.

For small rubber displacements (in a uni-axial strain loading) the following relation can be used (Rivlin 1948)

$$\epsilon_x = -\partial\xi/\partial X_0, \tag{26}$$

where ξ is the displacement magnitude in the x-direction and ϵ_x is the strain in the x-direction. Furthermore (see figure 2)

$$\lambda_x = \frac{\partial S}{\partial X_0} = \frac{\partial}{\partial X_0}(X_0 + \xi) = 1 - \epsilon_x. \tag{27}$$

When the rubber is free to expand in the y-direction its extension ratio in the y-direction, is given by

$$\lambda_y = 1 + \nu\epsilon_x, \tag{28}$$

where ν is the Poisson ratio defined as $\nu = -\epsilon_y/\epsilon_x$.

It was shown that for a uni-axial stress condition, in the absence of lateral inertia, the following stress–strain relation holds

$$\sigma_{tx} = G(\lambda_x^2 - \lambda_y^2). \tag{29}$$

Inserting (27) and (28) in (29) yields,

$$\sigma_{tx} = G[(1-\epsilon_x)^2 - (1+\nu\epsilon_x)^2]. \tag{30}$$

Rearranging (30) and neglecting second-order terms results in the following approximation,

$$\sigma_{tx} = 2G(1+\nu)\,\epsilon_x. \tag{31}$$

In a uni-axial strain case (figure 1*c*) the rubber cross section does not change ($A_{r0} = A_r$) and therefore, $\sigma_x = \sigma_{tx}$. When the rubber's Young modulus is $E = 2G(1+\nu)$ the expected hookean behaviour is obtained, i.e. $\sigma_x = E\epsilon_x$ for tension and $\sigma_x = -E\epsilon_x$ for compression. Although the preceding results were obtained on the basis of small displacements while considering a uni-axial stress condition, they are applicable to a uni-axial strain case since at small displacements the rubber deformation in the y and z axis is practically non-existent and therefore the neglection of the lateral inertia is fully justified.

The fact that for a uni-axial strain case the rubber behaves like a linear elastic material (under the assumption of small displacements) allows us to use the extended Hooke law, i.e.

$$\left.\begin{aligned} \epsilon_x &= (1/E)\,[\sigma_x - \nu(\sigma_y + \sigma_z)], \\ \epsilon_y &= (1/E)\,[\sigma_y - \nu(\sigma_x + \sigma_z)], \\ \epsilon_z &= (1/E)\,[\sigma_z - \nu(\sigma_x + \sigma_y)]. \end{aligned}\right\} \tag{32}$$

Furthermore, in a uni-axial strain case $\epsilon_z = \epsilon_y = 0$. Introducing these values into (32) results in

$$\sigma_x = -E\,\epsilon_x/[1 - 2\nu^2/(1-\nu)]. \tag{33}$$

Note that since we are dealing with compression, and not tension, a minus sign appears in the above equation.

In (33) the Young modulus E, is equal to $2G(1+\nu)$; (33) can therefore be rewritten as

$$\sigma_x(h_r, t) = \frac{2G(1+\nu)}{1-2\nu^2/(1-\nu)}[\lambda_x(h_r, t)-1]. \tag{34}$$

The stresses in the y- and z-directions can easily be obtained for the present condition (from (32)). They are

$$\sigma_y(h_r, t) = \sigma_z(h_r, t) = \frac{\nu}{1-\nu}\sigma_x(h_r, t) = \frac{2G\nu(1+\nu)}{1-\nu-2\nu^2}[\lambda_x(h_r, t)-1]. \tag{35}$$

It is evident from (34) that at the limit of $\nu \to \frac{1}{2}$, $\sigma_x \to \infty$ which means that deforming an incompressible material ($\nu = \frac{1}{2}$) requires an infinitely larger force.

Equations (1), (2), (4), (5), (6), (8), (9), (11), (16) and (22), (24) or (34) for a uni-axial stress case, a bi-axial stress case or a uni-axial strain case provide us with a set of ten equations for the following ten dependent variables: ρ_g, P, T, U_g, X, σ_x, λ_x, S, A_r and U_r. The independent variables are h_g and t for the gaseous phase and h_r and t for the rubber. These equations have to be solved simultaneously for the following boundary conditions:

$$U_g(h_g = H_g, t) = U_r(h_r = 0, t) = U_d(t), \tag{36}$$

$$U_r(h_r = H_r, t) = 0, \tag{37}$$

where $U_g(h_g = H_g, t)$ is the gaseous phase flow velocity at the solid plate d, at time t; H_g is the total mass of the gas which is contained between some reference section and the plate; $U_r(h_r = 0, t)$ is the velocity of the rubber leading edge (attached to the plate d) at time t, and U_d is the velocity of the solid plate. The value of U_d can be evaluated from the following equation;

$$w_d\, \mathrm{d}U_d(t)/\mathrm{d}t = P(h_g = H_g, t)\, A_g - |\sigma_x(h_r = 0, t)|\, A_{r0} - P_1(A_g - A_r), \tag{38}$$

where P_1 is the gas pressure (atmospheric) behind the rubber supported plate.

$U_r(h_r = H_r, t)$ is the velocity of the rubber trailing edge at time t and H_r is the total mass of the rubber. Since it is attached to a rigid, stationary wall this velocity must be zero.

Before attempting a solution of the previously described governing equations, the set was transferred to a non-dimensional form using the following definitions (asterisk indicates non-dimensional quantities)

$$t_g^* = \frac{ta_1}{L_1}, \quad t_r^* = \frac{tc_0}{L_{r0}}, \quad P^* = \frac{P}{\rho_{g1}a_1^2}, \quad \sigma^* = \frac{\sigma}{\rho_{r0}c_0^2}, \quad \rho_g^* = \frac{\rho_g}{\rho_{g1}}, \quad \rho_r^* = \frac{\rho_r}{\rho_{r0}} = 1,$$

$$x^* = \frac{x}{L_1}, \quad S^* = \frac{S}{L_{r0}}, \quad U_g^* = \frac{U_g}{a_1}, \quad U_r^* = \frac{U_r}{c_0}, \quad T^* = \frac{C_v T}{a_1^2}, \quad A_r^* = \frac{A_r}{A_{r0}},$$

$$h_g^* = \frac{h_g}{\rho_{g1}L_1A_g}, \quad h_r^* = \frac{h_r}{\rho_{r0}L_{r0}A_{r0}},$$

where indices 0 and 1 indicate pre-shock conditions in the rubber and the gas, respectively. L_1 is some reference length in the gas, a_1 and c_0 are the undisturbed speed of sound in the gas and the rubber, respectively. Other variables have been

defined earlier. In order to use only one non-dimensional time t^*, for both phases, the reference length in the gas was chosen to be: $L_1 = L_{r0}\, a_1/c_0$. The resulting set of non-dimensional, conservation equations is the following.

Conservation of mass in the gas:

$$\frac{\partial}{\partial t^*}\left[\rho_g^*(h_g^*, t^*)\frac{\partial x^*(h_g^*, t^*)}{\partial h_g^*}\right] = 0. \tag{39}$$

Definition of the gas velocity:

$$U_g^*(h_g^*, t^*) = \partial x^*(h_g^*, t^*)/\partial t^*. \tag{40}$$

Conservation of momentum in the gas:

$$\partial U_g^*(h_g^*, t^*)/\partial t^* = -\partial P^*(h_g^*, t^*)/\partial h_g^*. \tag{41}$$

Conservation of energy in the gas:

$$\partial T^*(h_g^*, t^*)/\partial t^* = -P^*(h_g^*, t^*)\,\partial V_g^*(h_g^*, t^*)/\partial t^*. \tag{42}$$

Equation of state for the gas:

$$P(h_g^*, t^*) = (\gamma - 1)\, T^*(h_g^*, t^*)/V_g^*(h_g^*, t^*). \tag{43}$$

Conservation of mass for an incompressible rubber (i.e. $\rho_r^* = 1$):

$$\frac{\partial}{\partial t^*}\left[\frac{\partial S^*(h_r^*, t^*)}{\partial h_r^*} A_r^*(h_r^*, t^*)\right] = 0. \tag{44}$$

Definition of velocity in the rubber:

$$U_r^*(h_r^*, t^*) = \partial S^*(h_r^*, t^*)/\partial t^*. \tag{45}$$

Definition of the extension ratio in the rubber:

$$\lambda_x(h_r^*, t^*) = \partial S^*(h_r^*, t^*)/\partial h_r^*. \tag{46}$$

(Note that λ is non-dimensional by definition.)

Conservation of momentum in the rubber:

$$\partial U_r^*(h_r^*, t^*)/\partial t^* = -\partial|\sigma_x^*(h_r^*, t^*)|/\partial h_r^*; \tag{47}$$

and an additional constitutive equation, depending upon the loading mode, i.e. for a uni-axial stress loading:

$$\sigma_x^*(h_r^*, t^*) = (G/\rho_{r0}\, c_0^2)\,[\lambda_x(h_r^*, t^*) - \lambda_x^{-2}(h_r^*, t^*)]; \tag{48a}$$

for a bi-axial stress loading:

$$\sigma_x^*(h_r^*, t^*) = (G/\rho_{r0}\, c_0^2)\,[\lambda_x(h_r^*, t^*) - \lambda_x^{-3}(h_r^*, t^*)]; \tag{48b}$$

for a uni-axial strain loading:

$$\sigma_x^*(h_r^*, t^*) = \frac{2G[1+\nu]}{\rho_{r0}\, c_0^2[1 - 2\nu^2/(1-\nu)]}[\lambda_x(h_r^*, t^*) - 1]. \tag{48c}$$

Equations (39) to (48) contain eight partial differential equations and two algebraic equations for the following ten dependent variables: ρ_g^*, P^*, T^*, U_g^*, X^*, σ_x^*, λ_x, S^*, A_r^* and U_r^*. The independent variables are: h_g^* and t^* for the gas and h_r^* and t^* for the rubber. This set of non-dimensional equations should be solved for the boundary

conditions given in (36) to (38). These boundary conditions, in a non-dimensional form, are

$$U_g^*\left(h_g^* = \frac{H_g}{\rho_{g1} L_1 A_g}, t^*\right) = \frac{c_0 U_r^*(h_r^* = 0, t^*)}{a_1} = \frac{c_0}{a_1} U_d^*(t^*), \tag{49}$$

$$U_r^*(h_r^* = 1, t^*) = 0. \tag{50}$$

U_d^* can be evaluated from the following equation,

$$\frac{w_d}{L_{r0}\rho_{r0}A_{r0}} \frac{dU_d^*}{dt^*} = \frac{\rho_{g1} a_1^2}{\rho_{r0} c_0^2} \frac{A_g}{A_{r0}} P^*\left(h_g^* = \frac{H_g}{\rho_{g1} L_1 A_g}, t^*\right) - |\sigma_x^*(h_r^* = 0, t^*)| - \frac{P_1}{\rho_{r0} c_0^2}\left(\frac{A_g}{A_{r0}} - A_r^*\right). \tag{51}$$

It is apparent from (39) to (51) that the following non-dimensional parameters characterize the flow field resulting from the head-on collision of a normal shock wave with a rubber supported rigid wall.

$w_d/(\rho_{r0} L_{r0} A_{r0})$, the ratio between the plate mass and the rubber mass.

$\rho_{g1} a_1/(\rho_{r0} c_0)$, the ratio between the gas and the rubber acoustic impedances.

a_1/c_0, the gas–rubber speed of sound ratio.

A_g/A_{r0}, the area ratio between the gas flow cross section and the initial rubber cross section.

$G/(\rho_{r0} c_0^2)$, the ratio between the rubber elasticity constant and the 'dynamic pressure' in the rubber.

$\gamma = C_p/C_v$, the specific heats ratio of the gas.

In addition, it is obvious that the incident shock wave Mach number, $M_s = V_s/a_1$, is also an important parameter.

3. The numerical scheme

Equations (39) to (48) form a set of partial differential equations that cannot be solved analytically. Therefore, a numerical scheme should be applied. Over the past 40 years a few schemes were developed that can handle flow discontinuities. In particular, the concepts of artificial viscosity (von Neumann & Richtmeyer 1950), the flux corrected transport (Boris & Book 1973) and the characteristic-based methods (Godonov 1959; Glimm 1965) gave rise to a variety of useful tools for obtaining numerical solutions for gas-dynamic equations. In the current research, the artificial viscosity method is used. Written in lagrangian coordinates, the resulting numerical scheme is convenient in handling moving interfaces such as that between the gas and the rubber. In addition, a wide class of constitutive relations for the rubber can be treated with the same scheme.

Some examples for using the artificial viscosity method can be found in the papers of Brode (1955), Boyer *et al.* (1958), Boyer (1959), Brode (1959), and Rakib *et al.* (1989).

When introducing the artificial viscosity terms into the governing equations only the momentum and energy equations are modified. The two latter are given subsequently (for simplicity, the asterisks were removed).

For the gaseous medium:

Conservation of momentum:

$$\frac{\partial U_g(h_g, t)}{\partial t} = -\frac{\partial}{\partial h_g}[P(h_g, t) + q_g(h_g, t)]. \tag{52}$$

Conservation of energy:

$$\partial T(h_g, t)/\partial t = -[P(h_g, t) + q_g(h_g, t)]\,\partial V_g(h_g, t)/\partial t, \tag{53}$$

where the artificial viscous pressure term for the gas is

$$q_g = \begin{cases} \dfrac{[C_g\,\Delta h_g]^2}{V_g(h_g, t)}\left[\dfrac{\partial V_g(h_g, t)}{\partial t}\right]^2 & \text{when} \quad \dfrac{\partial V_g(h_g, t)}{\partial t} < 0, \\ 0 & \text{when} \quad \dfrac{\partial V_g(h_g, t)}{\partial t} \geqslant 0, \end{cases} \tag{54}$$

where C_g is a non-dimensional constant which controls the shock wave thickness in the gas. The commonly used values for C_g are between 1.5 and 2, thus extending the shocks over 3 to 5 intervals of Δh_g. It can be seen from equation (54) that the effect of the artificial viscous pressure term q_g is significant only in the shock regions.

For the rubber:

Conservation of momentum:

$$\frac{\partial U_r(h_r, t)}{\partial t} = -\frac{\partial}{\partial h_r}[|\sigma_x(h_r, t)| + q_r(h_r, t)], \tag{55}$$

where the artificial viscous pressure term for the rubber is

$$q_r = \begin{cases} \dfrac{[C_r\,\Delta h_r]^2}{\lambda_x(h_r, t)}\left[\dfrac{\partial \lambda_x(h_r, t)}{\partial t}\right]^2 & \text{when} \quad \dfrac{\partial \lambda_x(h_r, t)}{\partial t} < 0, \\ 0 & \text{when} \quad \partial \lambda_x(h_r, t)/\partial t \geqslant 0, \end{cases} \tag{56}$$

where C_r is a non-dimensional constant.

Equations (39), (40), (52), (53), (54), (43), (44), (45), (46), (55) and (56) are converted into a set of central finite difference equations. As a result, a solution of second-order accuracy in space and time (i.e. $0[\Delta t]^2 + 0[\Delta h]^2$) is obtained. Thus knowing all the fluid properties up to (and including) some time $t = n\Delta T$, where n is an integer, it is possible to calculate the fluid properties at the next time level, i.e. $t = (n+1)\,\Delta t$. For the spatial differencing, a staggered grid is used. The velocity and the eulerian distance are computed at $J\Delta h$, while the rest of the fluid properties, such as pressure and density, are calculated at $(J+\frac{1}{2})\,\Delta h$, where $J = 1, 2, \ldots, N$ and N is the total number of space intervals. Details regarding the numerical scheme can be found in Mazor (1989).

4. Results and discussion

The numerical scheme was used first for solving the case of head-on collision of a normal shock wave with a rigid wall. This type of flow has an analytical solution and the obtained numerical results agreed very well with the analytical solution.

In the following the results obtained for the case of a head-on collision between a normal shock wave, propagating originally into a quiescent gas, and thereafter colliding with a rubber supported rigid plate are shown and discussed. The solution was obtained for an incident shock wave Mach number $M_s = 1.75$. The initial flow and rubber conditions were as follows: $P_1 = 1$ bar†, $U_{g1} = 0$, $T_1 = 300$ K, $\sigma_{t1} = 1$ bar and $U_{r0} = 0$. The solution was conducted for three different modes of rubber loading, i.e. uni-axial stress, bi-axial stress and uni-axial strain conditions. For all cases the

† 1 bar = 10^5 Pa.

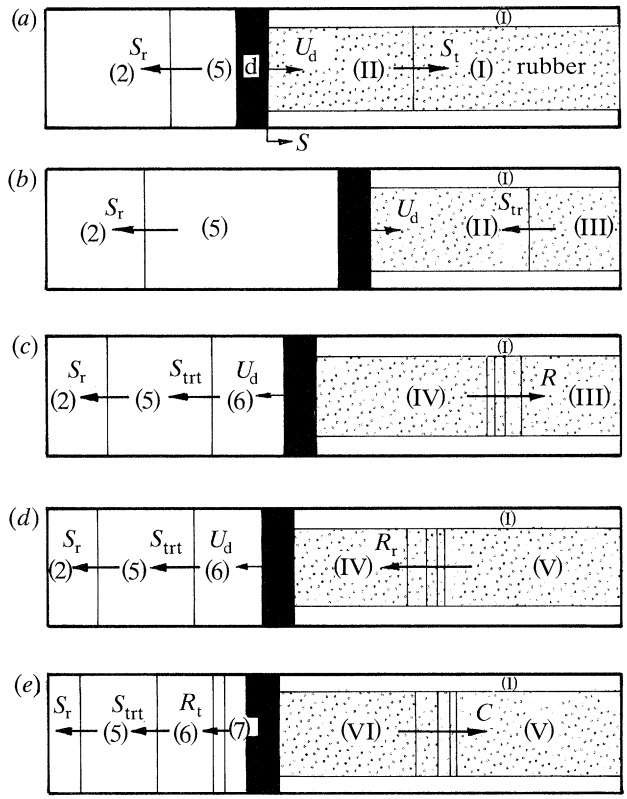

Figure 4. Schematic description of the wave patterns, in the gas and in the rubber, that resulted from the head-on collision between a normal shock wave and the rubber-supported plate.

following rubber physical properties were used: rubber initial length, $L_{r0} = 0.25$ m; ratio between the flow cross-sectional area (gas) and the initial rubber–rod cross section, $A_g/A_{r0} = 2$ (unlike the schematic description shown in figure 1*c*); rubber–metal-plate mass ratio $w_r/w_d = 20$; initial rubber density, $\rho_{r0} = 930$ kg m^{-3}, rubber's speed of sound, $c_0 = 46$ m s^{-1}, $G = 4$ bar and $\nu = 0.495$. For the cases of uni- and bi-axial stress loadings, the pressure in the gas surrounding the rubber, behind the plate, was kept constant and equal to the atmospheric pressure.

Before presenting detailed results, it is worthwhile to describe the shock wave collision process with the rubber supported plate qualitatively. This process is shown schematically in figure 4. Immediately after the collision (figure 4*a*) the incident shock wave is reflected backwards as a shock wave S_r and a transmitted shock wave S_t, propagates into the rubber rod. (Originally compression waves are transmitted into the rubber. However, as will be shown subsequently, these compression waves quickly coalesce into a shock wave.) The reflected shock wave S_r, changes the gas properties from state (2) to state (5), and the transmitted shock wave S_t, changes the rubber properties from state I to state II. Due to the high pressure behind the reflected shock wave P_5, the plate d is accelerated. The plate assumes a velocity U_d. Once the transmitted shock wave reaches the rubber's rear end, it is reflected (shock wave S_{tr} in figure 4*b*) into state II and changes it to a new state, state III. Until the shock wave (S_{tr}) reaches the rubber's leading edge, the plate d continues to move

from left to right and the rubber length is constantly reduced. Once the reflected shock wave S_{tr}, reaches the rubber's leading edge, it is reflected backward as a rarefaction wave, R, and a shock wave S_{trt} is transmitted into the gas. At this point the rubber rod reaches its minimum length (and maximum compression). It is due to this fact that a rarefaction is reflected into the rubber, R, and the plate d changes its direction of motion; now it moves from right to left and the rubber expands back towards its original length (figure 4*c*). The transmitted shock wave S_{trt}, which follows the reflected shock wave S_r, (figure 4*c*) separates between two flow states, (5) and (6). When the rarefaction wave, which propagates in the rubber, reaches the rubber's rear-end, it is reflected as a rarefaction wave, R_r, which separates between state IV and a new state V (see figure 4*d*). Once it reaches the rubber leading edge, the rubber reaches its maximum extension and at that point $U_d = 0$. Thereafter, the direction of the rubber front velocity changes; i.e. it starts moving from left to right and is being compressed again. The rarefaction wave, R_r, is reflected from the rubber leading edge as a compression wave, C, and a transmitted rarefaction wave, R_t, is sent into the gas (figure 4*e*). The rarefaction wave, R_t, follows the transmitted shock wave S_{trt}; it separates between two flow states (6) and (7), see figure 4*e*. In the rubber compression process, maximum stress is expected as state III (figure 4*b* and *c*). The highest pressure in the gas is experienced in state (6) (figure 4*c* and *d*).

When the incident shock wave hits the rubber supported plate, and reflects (as S_r, see figure 4*a*), compression waves propagate into the rubber. These compression waves coalesce into a shock wave. It is of interest to know when and where this change takes place.

Each pulse in the compression wave, called also a Riemann wave, propagates at a velocity c given by (Nowinski 1965)

$$c = u_s + \lambda c_0, \tag{57}$$

where

$$c_0 = ((1/\rho_{r0})\,\partial\sigma/\partial\lambda)^{\frac{1}{2}}; \tag{58}$$

c_0 is the disturbance shift rate, c is the absolute velocity of a Riemann wave and u_s is the absolute velocity of rubber particles. The other variables have been defined earlier.

The rubber stress–strain relation is the key to whether or not pressure pulses, generated at early times of the rubber compression, propagate slower than those generated at later times. When pulses generated at early times of the compression process propagate at a lower velocity than those produced at later times, the formation of a shock wave is imminent.

From the stress–strain relations given in (22) and (24) (for a uni- and a bi-axial loading cases, respectively) it is apparent that: $\partial\sigma_x/\partial\lambda_x > 0$ and $\partial^2\sigma_x/\partial\lambda_x^2 < 0$. These conditions guarantee that the compression waves coalesce into a shock wave; Nowinski (1965). Mazor *et al.* (1988) showed that the distance measured from the rubber–rod leading edge, at which the shock wave first appears S_s, is given by

$$S_s = c_0^2\, w_d / P_{5s} A_g. \tag{59}$$

The time required for this to happen (measured from moment the incident shock wave collided with the rubber-supported plate) can easily be deduced from the relation $S_s = c_0 t$.

In (59) P_{5s} indicates the pressure obtained behind the shock wave reflected from a rigid wall, w_d and A_g are the mass and cross-sectional area of the rubber-supported plate.

PHILOSOPHICAL TRANSACTIONS OF THE ROYAL SOCIETY A MATHEMATICAL, PHYSICAL & ENGINEERING SCIENCES

Figure 5

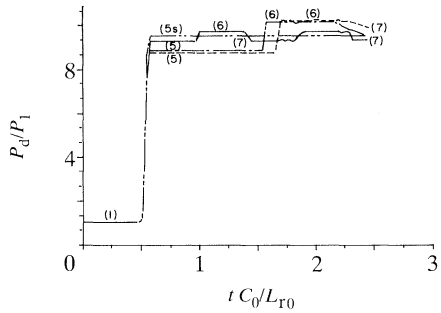

Figure 6

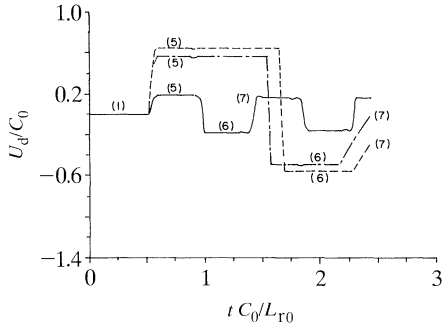

Figure 5. Gas pressure acting on the rubber supported plate as a function of time for different modes of rubber loading. ----, Uni-axial stress; ——, bi-axial stress; ——, uni-axial strain; —·—·—, rigid wall.

Figure 6. Velocity of the rubber supported plate as a function of time for different modes of rubber loading. ----, Uni-axial stress; ——, bi-axial stress; ——, uni-axial strain.

Figure 7

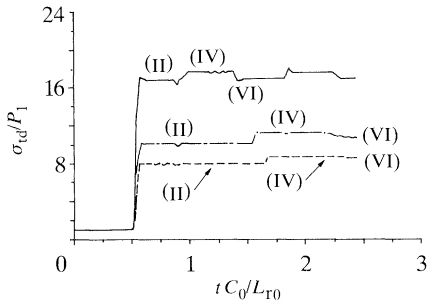

Figure 8

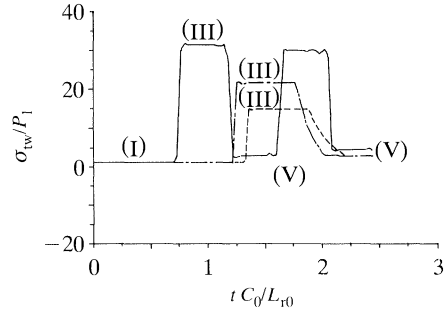

Figure 7. The stress at the rubber leading edge as a function of time for different modes of rubber loading. ----, Uni-axial stress; ——, bi-axial stress; —— uni-axial strain.

Figure 8. The rubber stress, at its rear-end, as a function of time for different modes of rubber loading. ----, Uni-axial stress; ——, bi-axial stress; ——, uni-axial strain.

For a given length L_{r0}, of a rubber rod it is clear that a shock wave, in the rubber, is expected when $L_{r0} > S_s$.

For a uni-axial strain loading it is apparent from (34) that $\partial\sigma_x/\partial\lambda_x = \text{const.}$, and therefore $\partial^2\sigma_x/\partial\lambda_x^2 = 0$. In this case the conditions needed for the coalescence of compression waves into a shock wave are not met and therefore, only compression waves exist throughout the rubber. It is clear from (34) and (57) that for such a case

$$c_0^2 = 2G(1+\nu)/\{\rho_{r0}[1-2\nu^2/(1-\nu)]\}.$$

Thus all disturbances move with the same velocity. This was also observed by Monti (1970) and Harding (1976), who referred to the head of these compression waves as a 'shock wave'.

(a) *Numerical results*

Some of the gas and the rubber properties at the various states (shown in figure 4) are shown quantitatively in figures 5 to 11 for the initial values given earlier. In figure 5 the pressure P_d/P_1, acting on the plate supported by the rubber rod, is shown as a function of the non-dimensional time tc_0/L_{r0}, for the three different rubber

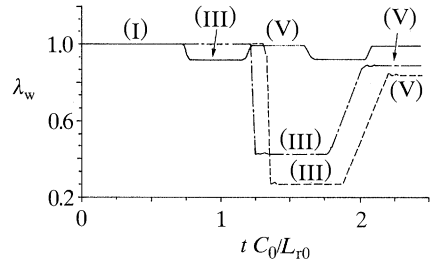

Figure 9. The rubber strain, at its rear-end, as a function of time for different modes of rubber loading. – – –, Uni-axial stress; – – –, bi-axial stress; ——, uni-axial strain.

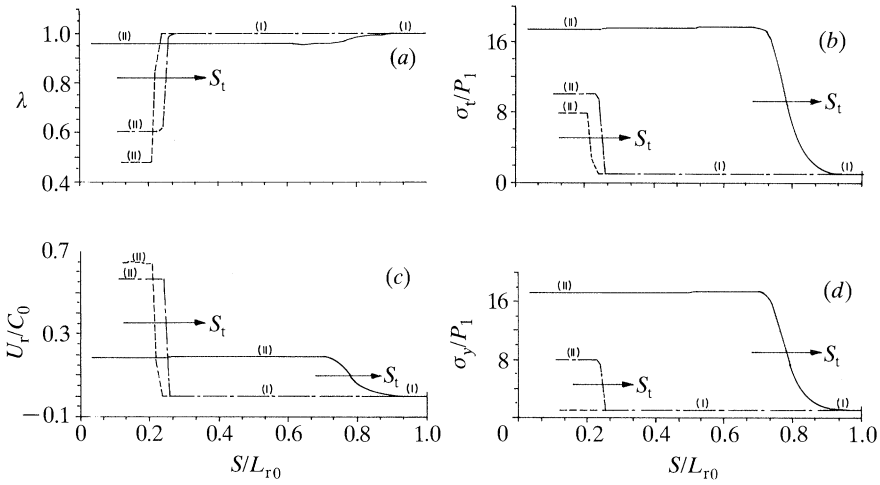

Figure 10. Changes in the rubber strain (*a*), stress (*b*), velocity (*c*) and stress in the *y*-direction, (*d*) as a function of distance at $t = 0.8$ ms after the head-on collision between the incident shock wave and the rubber-supported plate. – – –, Uni-axial stress; – – –, bi-axial stress; ——, uni-axial strain.

compression modes. For reference, the results obtained for a rigid wall are also shown. It is evident that the gas pressure acting on the plate goes through the following changes. Initially it is equal to P_1, then the reflected shock wave S_r, (see figure 4*a*) changes it to P_5. Thereafter, the transmitted shock wave S_{trt} (see figure 4*c*) changes it to P_6; and finally the transmitted rarefaction wave R_t (see figure 4*e*) changes it to P_7. While P_5 and P_6 remain constant, P_7 decreases monotonically. For all three loading modes the obtained values for P_5 are smaller than P_{5s}. P_{5s} is the pressure obtained behind a shock wave reflected from a rigid wall. The smallest value of P_5 is obtained in the uni-axial stress loading while the largest in the case of a uni-axial strain loading. On the other hand, in all the three loading modes P_6 is larger than P_{5s}. The largest P_6 is obtained in a uni-axial stress loading while the smallest in a uni-axial strain loading. It is also apparent from figure 5 that states (5) and (6) exist for a longer time in a uni-axial stress loading while the shortest duration belongs to the case of uni-axial strain loading.

The plate velocity (normalized by the speed of sound in the rubber, c_0) is shown as a function of non-dimensional time in figure 6. The changes in the plate velocity are clearly noticeable in this figure. Following the head-on collision the plate moves from left to right (positive velocity). This motion continues until the reflected shock wave

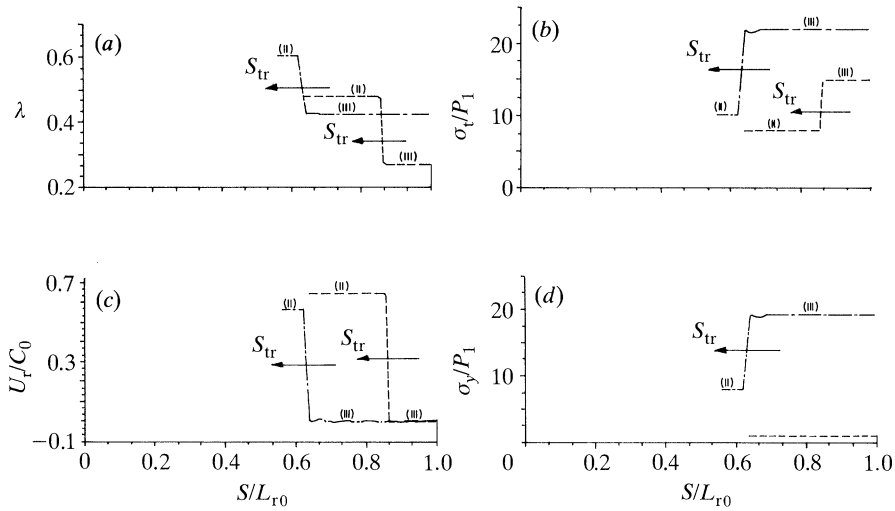

Figure 11. Changes in the rubber strain (*a*), stress (*b*), velocity (*c*) and stress in the *y*-direction, (*d*) as a function of distance at $t = 5$ ms after the head-on collision between the incident shock wave and the rubber-supported plate. ——, Uni-axial stress; — — —, bi-axial stress.

in the rubber S_{tr} (see figure 4*b*) reaches the plate. It stops the plate and imposes a motion from right to left (negative velocity). This motion continues until the reflected rarefaction wave in the rubber R_r, reaches the plate. When this occurs, the direction of motion of the rubber-supported plate is reversed. When the plate passes again through its original position it can be said that a cycle has been completed. It is apparent from figure 6 that the waves move with the highest velocities in the case of uni-axial strain loading since more cycles are completed for this case in a given time.

Variations in the rubber stress at its leading edge, where it is attached to the plate, are shown in figure 7. As could be expected, the largest stress is obtained for a uni-axial strain loading, while the smallest is obtained in a uni-axial stress loading. Since $A_g/A_{r0} = 2$, it is expected that σ_{td} will be higher than P_5 (shown in figure 5). It could be expected (based upon the results shown in figure 7) that the smallest strain (λ_d) be obtained for the uni-axial strain loading, while the largest would be reached for the uni-axial stress loading.

The stress (σ_{tw}) and strain (λ_w) experienced by the rubber at its rear-end, where it is attached to a rigid wall, are shown in figures 8 and 9, respectively. It is apparent from these figures that the largest stress, and the smallest strain are obtained for the uni-axial strain loading, while the smallest stress and the largest strain, at the rubber rear-end, are obtained for the uni-axial stress loading. It should be noted that the stress experienced by the rubber at its rear-end is significantly larger than the gas pressure near the plate (P_5 and/or P_6, see figure 5). It is also significantly larger than the pressure obtained behind a reflected shock wave from a rigid wall under similar initial conditions. The fact that $\sigma_{t,III}$ is significantly larger than P_{5s} was also observed by Muirhead (1958), Monti (1970), Gelfand *et al.* (1975), Gelfand *et al.* (1984), and Gvozdeva *et al.* (1986).

The numerical results can also be presented as a function of distance for a given time. When the time is properly chosen, the changes in the flow/rubber properties through any of the shock or rarefaction waves shown schematically in figure 4 can

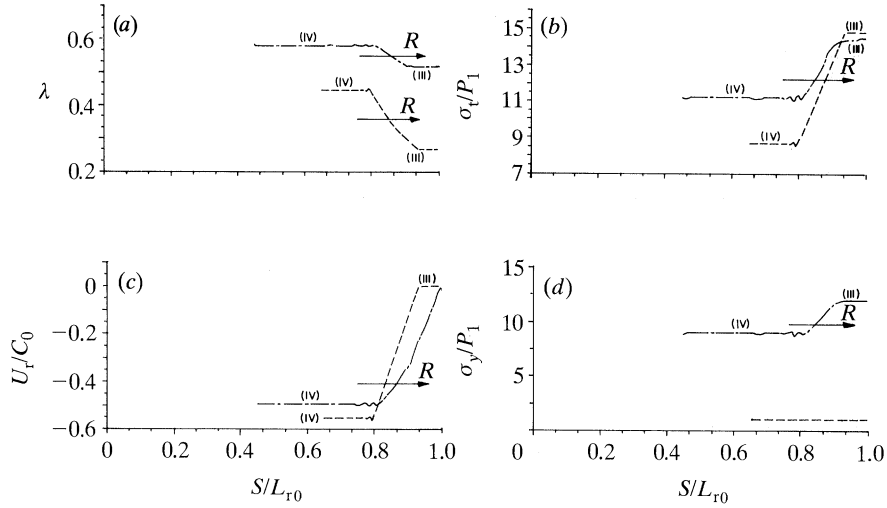

Figure 12. Changes in the rubber strain (*a*), stress (*b*), velocity (*c*) and stress in the *y*-direction, (*d*) as a function of distance at $t = 7$ ms after the head-on collision between the incident shock wave and the rubber-supported plate. ——, Uni-axial stress; ———, bi-axial stress.

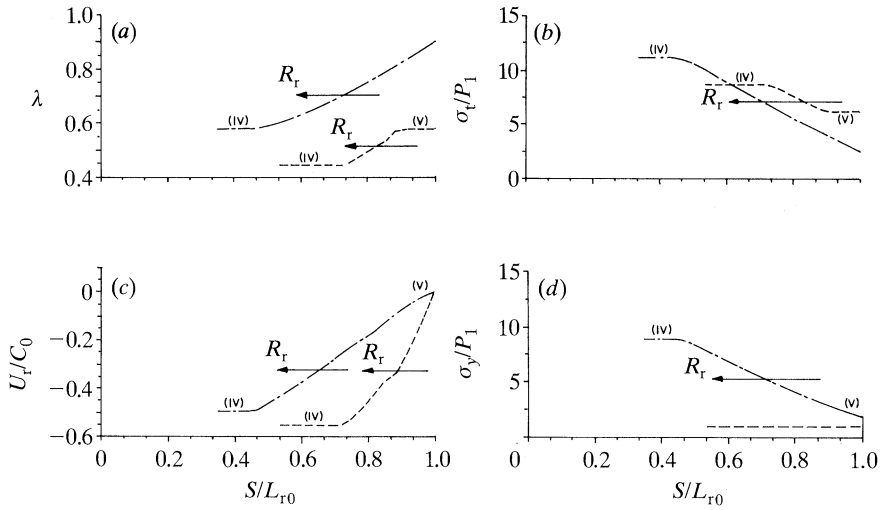

Figure 13. Changes in the rubber strain (*a*), stress (*b*), velocity (*c*) and stress in the *y*-direction, (*d*) as a function of distance at $t = 8.2$ ms after the head-on collision between the incident shock wave and the rubber-supported plate. ——, Uni-axial stress; ———, bi-axial stress.

be obtained. In the following, changes in the rubber strain λ, stress σ_t, velocity U_r, and stress in the *y*-direction σ_y, through S_t, S_{tr}, R and R_r are shown. The distance S is measured from the initial position of the plate, d. The initial conditions used for obtaining the results shown in figures 10 to 13 are identical to those used before (in figures 5–9). The results shown in figure 10*a–d* were obtained at an early time after the head-on collision between the incident shock wave and the rubber supported plate, i.e. $t = 0.8$ ms. At this early time the only discontinuity present in the rubber is the transmitted shock wave (S_t in figure 4*a*). As could be expected, the smallest strain (λ_{II}) and the largest stress (σ_{tII}) are experienced while applying a uni-axial

strain loading (figure 10*a*, *b*). Minimum rubber velocity and maximum stress in the y-direction are associated with a uni-axial strain loading (figure 10*c*, *d*). For a uni-axial stress loading one obtains the largest strain, λ, and rubber velocity, U_r, and the smallest stress, σ_t. For this case, by definition $\sigma_y = P_1$. It is also evident from figure 10*a–d* that, while in the uni- and bi-axial stress cases the transmitted wave is definitely a shock wave, for the uni-axial strain loading a compression wave is transmitted into the rubber rod. This compression wave moves much quicker than the shock waves produced in the uni- and bi-axial stress loading cases.

At a later time ($t = 5$ ms after the head-on collision) the transmitted wave has reached the rubber-rod rear-end and has been reflected back into the rubber as shown schematically in figure 4*b*. Owing to the fact that the wave propagation velocity is much smaller in the cases of uni- and bi-axial stress loading, relative to the case of uni-axial strain loading, a comparison of the three cases at this (and later) time is meaningless. This is so because at the considered time ($t = 5$ ms) the wave patterns in the cases of uni-axial and bi-axial stress loadings are those shown in figure 4*b*, while in a uni-axial strain loading the wave pattern of figure 4*c* exists. For this reason in figures 11 to 13 only the cases of uni- and bi-axial stress loadings are shown. In figure 11*a–d* the increase in the rubber strain (figure 11*a*) and stress (figure 11*b*) through the reflected shock wave, S_{tr}, and the decrease in the rubber velocity ($U_{rIII} = 0$, figure 11*c*) are shown. The increase in the y-component of the rubber stress through the reflected shock wave, is shown in figure 11*d*. By definition, $\sigma_y = P_1$ for a uni-axial stress loading. Larger changes in the rubber properties while crossing the reflected shock wave are experienced in the case of bi-axial stress loading.

Proceeding to a later time, after the head-on collision between the incident shock wave and the rubber supported plate ($t = 7$ ms) brings us to the wave pattern shown in figure 4*c*, that is, a reflected rarefaction wave R propagates into the rubber. This rarefaction wave and the changes in the rubber properties across it are clearly visible in figure 12*a–d*. As expected, the magnitude of the rubber strain and stress decrease across the rarefaction wave and its velocity increases (in an opposite direction to the wave propagation, see figure 12*c*). When the rubber properties presented in figure 12 are compared with appropriate properties shown before as a function of time, for example, σ_{tIII} in figure 12*b* with σ_w shown in figure 8, attention should be given to the following fact. In figure 8 the properties marked as III start, for a bi-axial stress loading case, at $tc_0/L_{r0} \approx 1.245$ and end at $tc_0/L_{r0} \approx 2.05$. It reaches a constant, plateau level for $1.3 < tc_0/L_{r0} < 1.55$. The results shown in figure 12*b* are given for $t = 7$ ms which corresponds to $tc_0/L_{r0} = 1.288$; that is, before reaching the plateau level and therefore, σ_{III} shown in figure 12*b* is smaller than the plateau level value of over 20 shown in figure 8.

Proceeding to a later time, $t = 8.2$ ms after the head-on collision, the wave pattern that appears in the rubber is the reflected rarefaction wave shown schematically in figure 4*d*. This wave, and the rubber properties across it are shown in figure 13*a–d*. The expected behaviour of a decrease in the rubber stress, strain and velocity (zero velocity at the rigid wall) is evident in these figures. Should one proceed to even later times, then the results typical to a compression wave (shown schematically in figure 4*e*) would be obtained (see Mazor 1989).

So far numerical results based on the physical model developed in the preceding section were presented. These results confirmed that the wave patterns in the gas and in the rubber, which are shown schematically in figure 4, exist. It also provides us with quantitative results regarding the gas and rubber properties across these waves.

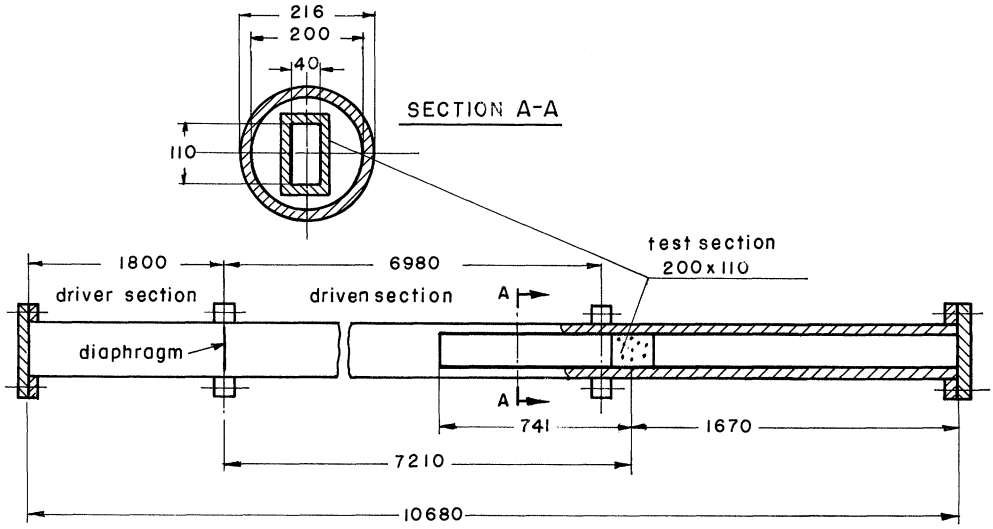

Figure 14. Schematic illustration of the EMI shock tube used for studying the interaction between an incident shock wave and the rubber-supported plate. Distances in millimetres.

To remove any doubts regarding the validity of the proposed physical model (summarized in (39) to (48)) and the numerical scheme used for its solution, it is necessary to compare the numerical results with appropriate experimental findings. This is the object of the following section.

(*b*) *Experimental results*

Experiments were conducted in the shock tube of the Ernst Mach Institute, Freiburg. This shock tube has an inner diameter of 20 cm. The driver section is 180 cm long, the driven section is 888 cm long and the test section is located about 721 cm downstream of the diaphragm. A schematic description of this tube is shown in figure 14. Cellulose acetate sheets were used as diaphragms for separating between the two sections. This was proven to be an excellent diaphragm material since it is brittle when stretched and has a high breaking velocity. The shock tube has a test section equipped with plane, parallel windows of high optical quality glass. The optical field of view is 200 mm × 110 mm and its depth is 40 mm. It is designed for using 'two-dimensional' models. During experiments the gas flow and the rubber behaviour were monitored by pressure measurements (using Kistler 606 pressure transducers) and by high-speed shadowgraph photography. The shadowgraphs were obtained with a 24 frame Cranz-Schardin Spark Camera. Twenty-four point spark sources are focused onto the 24 objectives of the camera by use of a concave mirror. At the instant of ignition a spark is projected onto the film through the objective into which the image of the spark was copied. The advantage of this photographic technique is the fact that there are no movable parts in the light rays path. Therefore, the optical resolution is determined only by the aperture of the objectives.

From the three different modes of rubber loading (shown schematically in figure 1) the one in which significant deformation takes place, and is relatively easy to investigate in a shock tube is the case of bi-axial stress loading. This case was investigated in the experiments to be described. It was shown earlier that the position where the transmitted compression waves coalesce into a shock wave is given by (59). Therefore, a transmitted shock wave will be present in the rubber only

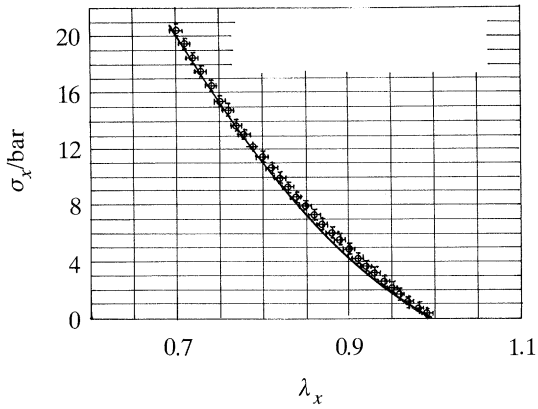

Figure 15. A statically obtained stress–strain relation for a rubber specimen under a bi-axial stress loading. ○, Experiments (bi-axial stress); ——, $\sigma_x = G|\lambda_x - \lambda_x^{-3}|$; ($G = 9.317$ bar).

if $L_{r0} > S_s$. The criterion whether a shock or a compression wave exists in the rubber depends upon the rubber physical properties (which influence c_0), the plate mass (w_d) and its size (A_g), and the incident shock wave Mach number (which dictates the value of P_{5g}). In choosing the rubber rod and the experimental conditions we tried to keep both options, i.e. obtaining either a compression or a shock wave in the rubber. The case when only compression waves exist in the rubber is easy to obtain; all that is needed is that $L_{r0} < S_s$. Choosing a heavy plate and a short rubber rod suffice to ensure this requirement. It is more difficult to ensure the existence of a shock wave in the rubber because choosing a too long rubber rod and/or a very light plate will result in the rubber buckling and the plate bending while carrying the incident shock wave produced load. Based upon the above-mentioned requirements and limitations, it was decided to use a rubber rod having a cross section of 4 cm × 4 cm, length of $L_{r0} = 10$ cm and density of 1014 kg m^{-3}. Its chemical composition is: natural rubber SMR 100.0 gr, stearine 2.0 gr, zinc oxide 5.0 gr, carbon black Haf 10.0 gr, antioxidant 224b 2.0 gr, sulphur 2.75 gr, CBS 1.00 gr, TMTD 0.10 gr. This composition ensured good elasticity; i.e. ability to experience large deformations. The chemical composition of the rubber determines the value of c_0. Thus, to cover, experimentally, the two cases described above, namely: a case in which the compression waves do not converge to a shock wave, and the case in which the compression waves coalesce into a shock wave, the other parameters, i.e. M_s, w_d and A_g had to be chosen properly. For obtaining a transmitted compression wave throughout the rubber, the following initial conditions were adopted: $M_s = 1.55$, $w_d = 0.123$ kg and $A_g = 0.0044$ m^2. This value of A_g is identical to the test-section cross-sectional area (4 cm × 11 cm). For obtaining the case where the transmitted compression wave coalesces into a shock wave, in the rubber, the following initial conditions were adopted: $M_s = 1.55$, $w_d = 0.032$ kg and $A_g = 0.0032$ m^2. The reduction of A_g was obtained with the aid of a cookey-cutter which was mounted in the test section as is shown in figure 16*b*.

To have a reliable stress–strain correlation, the manufactured rubber rod was compressed in an Instron machine under bi-axial stress loading conditions. The obtained results are shown in figure 15, a curve of the form $\sigma = G(\lambda - \lambda^{-3})$, appropriate to this type of loading, was fitted to these results. The maximum deviation of the experimental results from the proposed curve fit is about 5%. The fitted curve resulted in $G = 9.317$ bar.

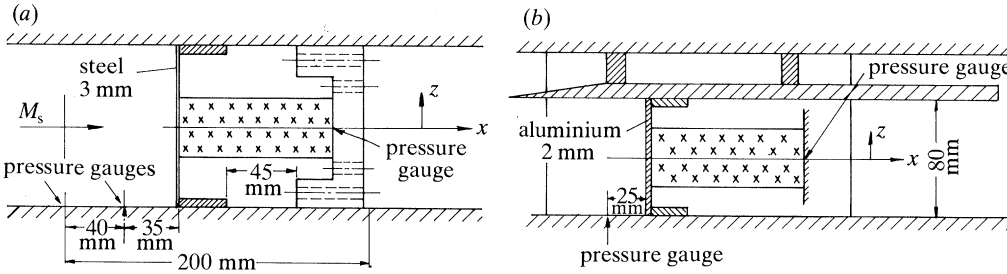

Figure 16. Illustration of the rubber-rod, and the plate it supports, positioned inside the shock tube test-section, (*a*) for obtaining a compression wave in the rubber, (*b*) for obtaining a shock wave in the rubber.

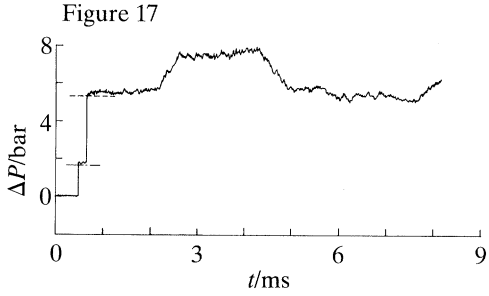

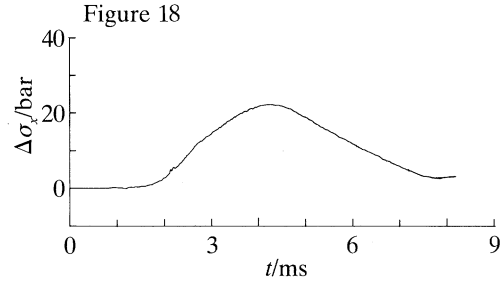

Figure 17. Pressure history on the rubber-supported plate. Analytical predictions: ----, P_5; ———, P_2.

Figure 18. Pressure history at the rubber's rear-end.

In a bi-axial stress loading the rubber is free to expand in only one direction. For reducing the friction between the rubber rod and the shock tube walls (windows), the entire contact surface was lubricated. Many experiments were conducted; in the following only two sets of results are shown. One for the case when the transmitted compression waves in the rubber rod do not coalesce into a shock wave, and one for the case when the compression waves do coalesce into a shock wave in the rubber. Schematic illustration showing the installation of the rubber rod and the plate it supports in the shock tube test section is shown in figure 16*a* and *b*.

We now consider the results of these two sets of experiments. The pressure variations as a function of time, measured 35 mm ahead of the rubber supported plate, are shown in figure 17. The initial conditions for this experiment were $T_1 = 294.7$ K, $P_1 = 0.99$ bar and the measured shock wave Mach number was 1.557. The rubber rod position in the considered experiment is shown in figure 16*a*. The pressure jump through the incident shock wave is clearly visible (at $t \approx 0.5$ ms). Thereafter, the constant pressure behind the reflected shock wave (S_r), P_5 can also be seen very clearly. Both P_2/P_1 and P_5/P_2 agree well with the analytically evaluated values for $M_s = 1.557$. The third pressure increase (a more gradual increase starting at $t \approx 2.2$ ms) is higher than the numerically predicted value for P_6. This pressure increase is most probably a result of wave interactions which occur in the shock tube; they are not included in the present numerical solution. It is clear from figure 16*b* that the flow cross section, of the tested gas, is reduced by the cookey-cutter. This cookey-cutter splits the incident shock wave into two parts; one propagates below it, towards the rubber supported plate, while the other propagates above it, towards the

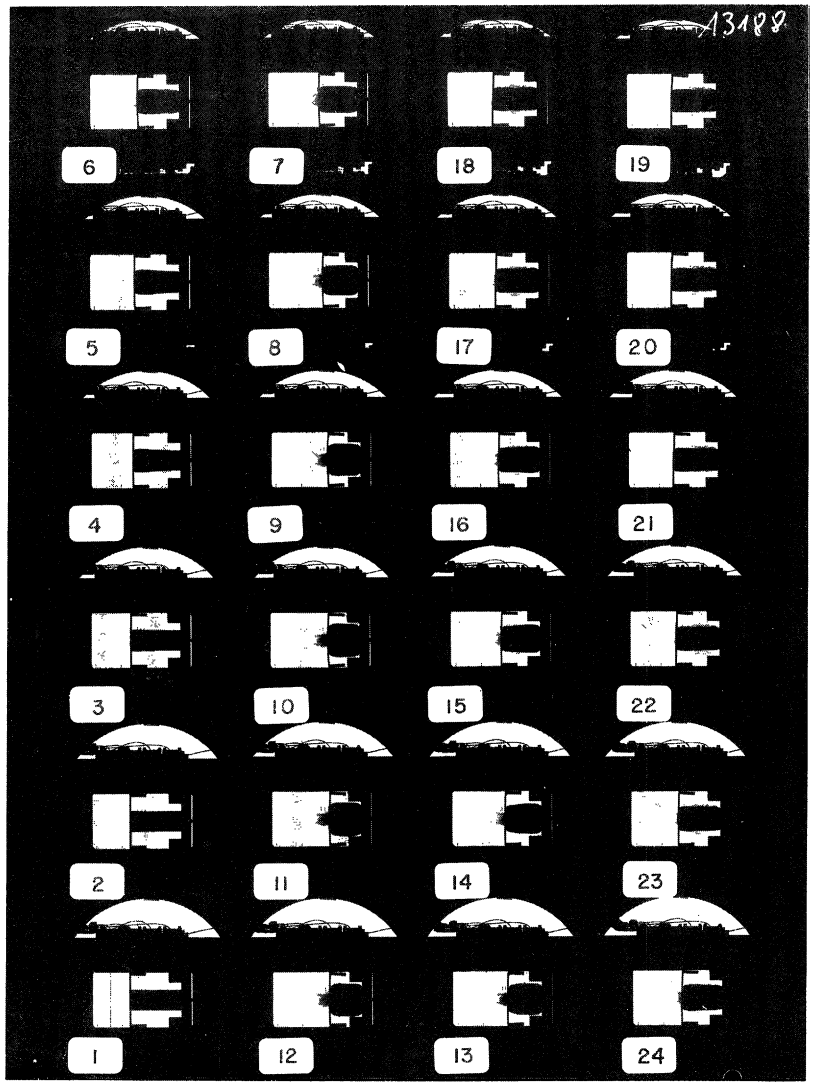

Figure 19. Shadowgraphs during and after the head-on collision between the incident shock wave and the rubber supported plate: The time elapsed between successive frames is 400 μs.

supports of the cookey-cutter. Since the first support of the cookey-cutter is closer to the cookey-cutter's leading edge than the rubber supported plate (see figure 16*b*), the shock wave which reflects from it reaches the leading edge of the cookey-cutter before the shock wave reflected from the rubber supported plate. Upon reaching the cookey-cutter's leading edge the first reflected shock wave diffracts over it. Part of this diffracted shock wave collides, head-on, with the shock wave which was reflected from the rubber supported plate. As a result of this collision a shock wave will move towards the plate and will influence the reading of the pressure gauge which is located near the rubber supported plate. Similar wave interactions are generated by the major cookey-cutter, which cuts-out the test-section (rectangular) from the circular driven section; see figure 14. In addition, head-on collision between the reflected shock wave and the contact surface also generates waves which move towards the

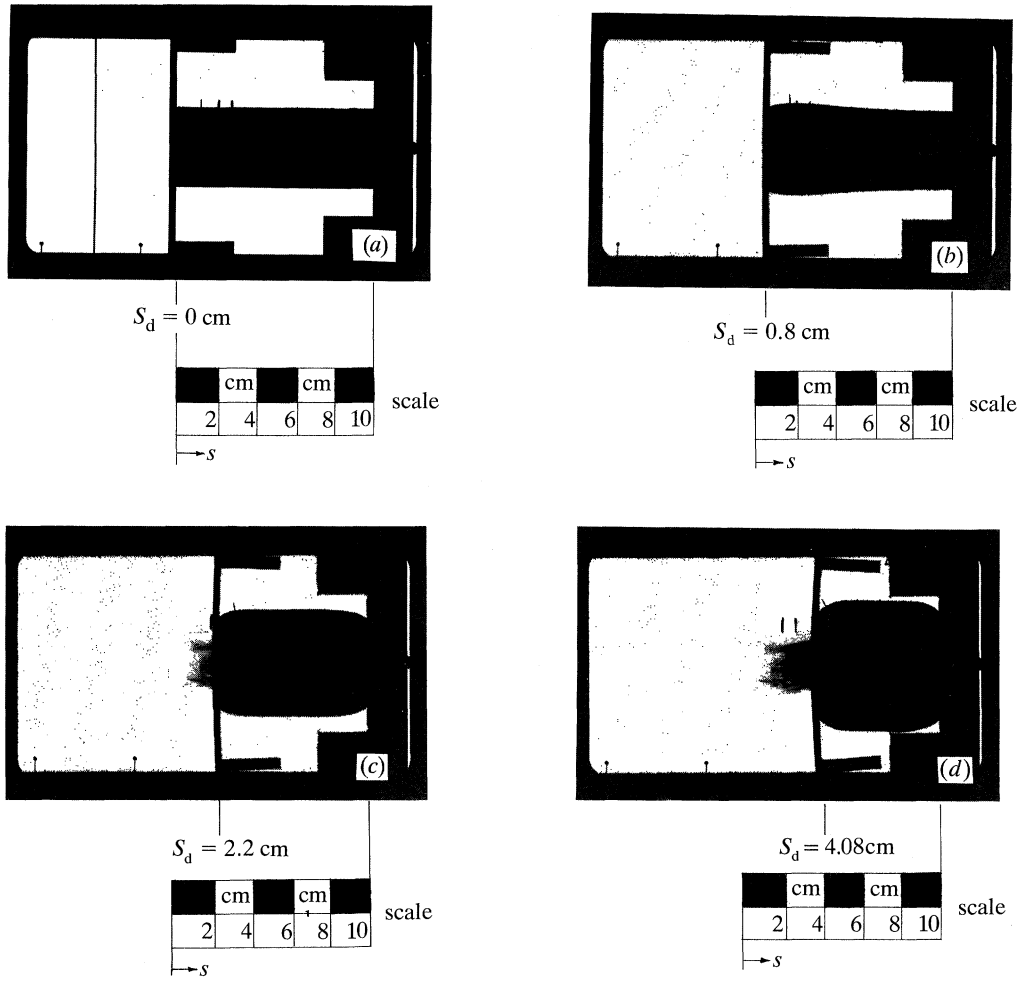

Figure 20. Enlargement of shadowgraphs of figure 19: (*a*) frame no. 1, $t = 2.78$ ms; (*b*) frame no. 4, $t = 4$ ms; (*c*) frame no. 7, $t = 5.2$ ms; (*d*) frame no. 11, $t = 6.8$ ms.

rubber-supported plate and affect the pressure field. All the above-mentioned interactions are not included in the numerical simulation. Therefore, comparison between experimental and numerical results should be limited, for the present experiment, to $t < 2$ ms, measured from the time S_r first appears.

The pressure (stress) recording at the rubber rod rear-end, where it is attached to a rigid wall, is shown in figure 18. It is clear that the pressure there increases gradually through the compression waves to a maximum and thereafter gradually decreases through the reflected rarefaction wave R_r. The maximum value of the rubber stress is almost five times higher than P_5 (see figures 17 and 18). When released, some residual stress remains in the rubber (figure 18).

The response of the rubber rod to the incident shock wave load is shown in figure 19. This figure is a set of successive shadowgraphs taken 0.4 ms apart. The numbers, 1–24, appearing in each frame indicate the time progress. At the first shadowgraph (no. 1 in figure 19) the incident shock wave is clearly seen just before it collides with the rubber-supported plate. All other frames show the rubber rod at different stages

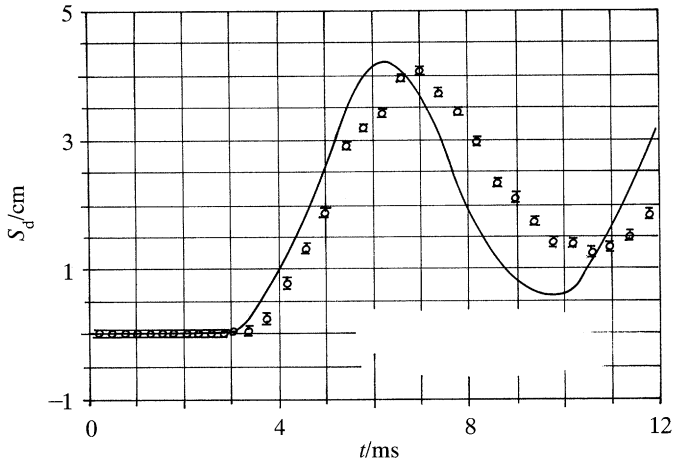

Figure 21. Displacement of the rubber-supported plate; ——, numerical results; ○, experimental findings.

of its loading and release processes. The rubber compression along the x-axis and its expansion along the z-axis are clearly visible in frames 3–11 of figure 19. Minimum length, in the x-direction, and maximum expansion in the z-direction are evident in the 11th frame (at about 4 ms after the head-on collision between the incident shock wave and the rubber supported plate). Thereafter, the rubber rod starts to expand in the x-direction due to the rarefaction wave which is reflected from its leading edge, see figure 4*c*. The dark stains shown in front of the plate in frames 7 to 15 and 24 of figure 19 are silicone grease traces used for lubricating the rubber slide on the shock tube windows. In addition to the expected behaviour of the rubber rod, which is shown qualitatively in figure 19, one may obtain quantitative results of the rubber's front displacements during its loading and release processes. This can be done by measuring the position of the plate at different times, see figure 20. It is apparent from this figure that the length of the rubber rod was reduced to about 60% of its original length; this is quite a large deformation.

One of the assumptions used in the model proposed for the rubber behaviour was that the rubber is incompressible. Because of this assumption, in a bi-axial stress loading, $\lambda_z = 1/\lambda_x$. From the results shown in figure 20 the validity of this assumption can be checked. In figure 20*d*, where the rubber at about 4 ms after its collision with the incident shock wave is shown, the rubber reached its maximum compression; i.e. its original length is reduced by 4.08 cm. Therefore, $\lambda_x = (10-4.08)/10 = 0.592$. At this time the rubber experiences its maximum expansion in the z-direction, which is $\Delta\lambda_z = 2.75$. Therefore, $\lambda_z = (4+2.75)/4 = 1.688$. These values of λ_x and λ_z perfectly agree with the incompressible condition, i.e. $\lambda_x\lambda_z = 1$.

The above-discussed experiment was simulated using the physical model and the numerical code described earlier. The numerical results obtained for the displacement of the rubber-rod leading edge S_d, are shown in figure 21 as a solid line. The experimental findings appear as small circles. The short lines above and below each circle indicate the range of the experimental error involved in measuring S_d. Good agreement between experimental and numerical results is obtained for times $t < 5.5$ ms. The reason for the difference between the two results is mainly due to the

PHILOSOPHICAL TRANSACTIONS OF THE ROYAL SOCIETY A MATHEMATICAL, PHYSICAL & ENGINEERING SCIENCES

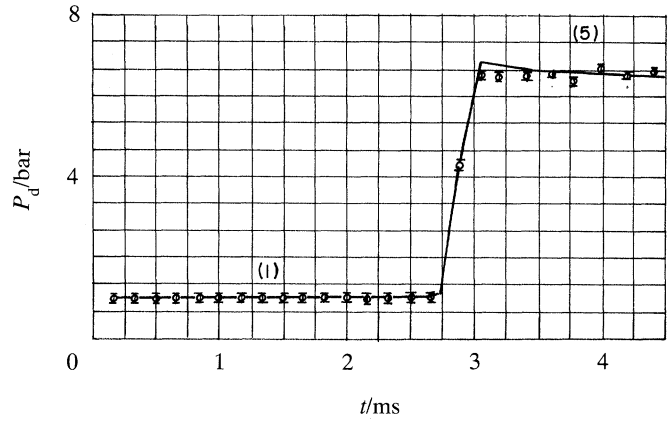

Figure 22. The gas pressure acting on the rubber-supported plate; ——, numerical results; ○, experimental findings.

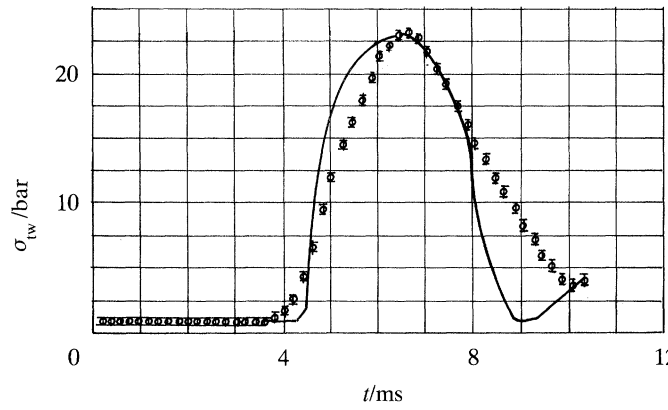

Figure 23. The stress at the rubber rear-end where it is attached to a rigid wall; ——, numerical results; ○, experimental findings.

fact that in the numerical solution friction between the rubber rod and the shock tube windows was neglected. (In addition, the interaction between the reflected shock wave, S_t, and the contact surface is not included in the numerical solution.) Apparently, in spite of the lubrication used, at a high rubber compression the force pressing the rubber to the windows is large and neglecting the friction force is not justified. It should be noted that both the experimental and the numerical results exhibit the same trend, i.e. similar amplitude and time period. It is very clear from the experimental results that at the end of the pressure release (completion of one cycle) the rubber rod does not return to its original length.

A comparison between the experimental and the numerical results obtained for the gas pressure on the rubber-supported plate P_d, is shown in figure 22. Very good agreement is evident in the time duration shown in this figure.

A comparison between the experimental and the numerical findings for the rubber stress, at its rear end where it is attached to a rigid wall, is given in figure 23. It is evident from this figure that the head of the compression wave reaches the rear-end of the rubber earlier in the actual experiment than in the numerical simulation. This fact suggests that the actual value of G, which determines the wave propagation

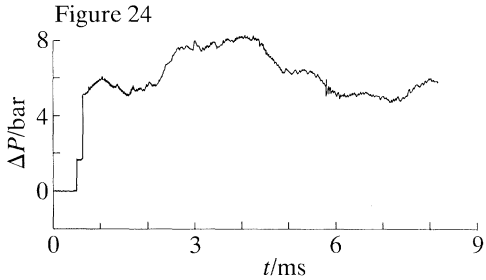

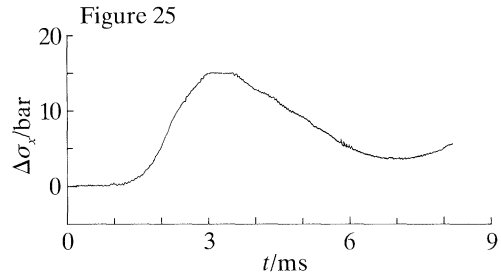

Figure 24. Pressure history on the rubber-supported plate.

Figure 25. Pressure history at the rubber's rear-end.

velocity in the rubber, is slightly larger than the value used in the numerical simulation. The latter was deduced from static loading of the used rubber rod. It is possible that a different value for G should be used for a dynamic loading, or that the value of G has slightly changed due to previous experiments with the rubber rod.

The second set of experimental results were obtained for a case when the transmitted compression waves coalesce into a shock wave in the rubber. The installation of the rubber rod in the shock tube test section is shown schematically in figure 16*b*. The initial conditions used in this experiment are: $P_1 = 0.996$ bar, $T_1 = 294.8$ K, $A_g = 0.0032$ m^2 and the measured incident shock wave Mach number was $M_s = 1.562$. The rubber geometry and chemical composition were the same as in the previously described case.

The pressure history on the rubber supported plate is shown in figure 24. The pressure jumps through the incident and the reflected shock waves are clearly visible in this figure. These jumps agree well with the values calculated analytically using $M_s = 1.562$ and $P_1 = 0.996$ bar. Again, the pressures measured at $t > 2$ ms, in figure 24, are higher than the numerically predicted values for P_6. This is due to wave interactions in the shock tube which are not included in the physical model presented earlier.

The pressure history (stress) at the rubber rear-end, where it is attached to a rigid wall, is shown in figure 25. The plateau seen in the figure at $3 \leqslant t \leqslant 3.75$ ms, which was not observed in figure 18, is a clear evidence that a shock wave is reflected from the rear-end of the rubber rod. Comparing figure 25 with 18 indicates that the pressure (stress) rise in the former is quicker, and the pressure variations with time is less symmetric than that shown in figure 18. This is a further indication that a shock wave has been formed in the case described in figure 25, while a compression wave existed in figure 18.

The rubber behaviour under loading, at different times, is shown in the shadowgraph photographs of figure 26. In figure 26*a* the time interval between successive frames is 25 μs; the total time covered in the flow history shown in this figure is 575 μs. In frames 1–3 the incident shock wave, prior to its head-on collision with the rubber supported plate, is seen. As should be expected, the rubber geometry is unchanged in these frames. The reflected shock wave, S_r, is visible in frames 4–11. The rubber response to the head-on collision with the incident shock wave is not instantaneous, as can be seen from figure 26*a*. The velocity of the incident shock wave can be deduced from frames 1–3 and that of the reflected shock wave from frames 4–11. They agree very well with the analytically predicted value for V_s and V_{sr}. For better visualizing the rubber deformation and measuring the plate displacement,

PHILOSOPHICAL TRANSACTIONS OF THE ROYAL SOCIETY A MATHEMATICAL, PHYSICAL & ENGINEERING SCIENCES

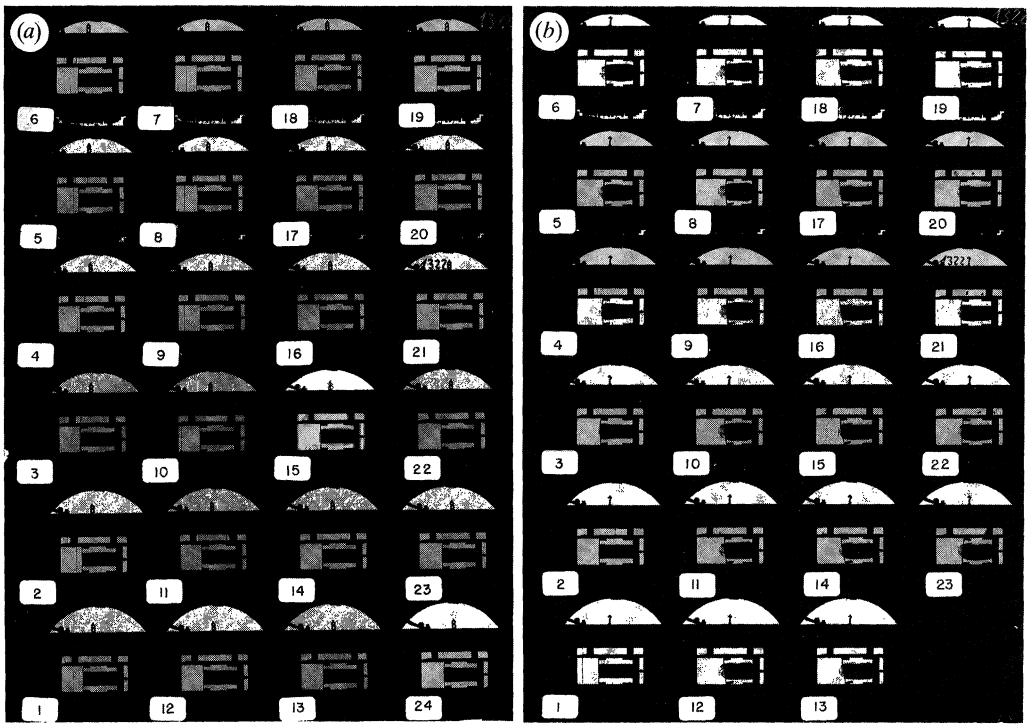

Figure 26. (*a*) Shadowgraphs during and after the head-on collision between the incident shock wave and the rubber-supported plate. The time elapsed between successive frames is 25 μs. (*b*) Shadowgraphs during and after the head-on collision between the incident shock wave and the rubber-supported plate. The time elapsed between successive frames is 400 μs.

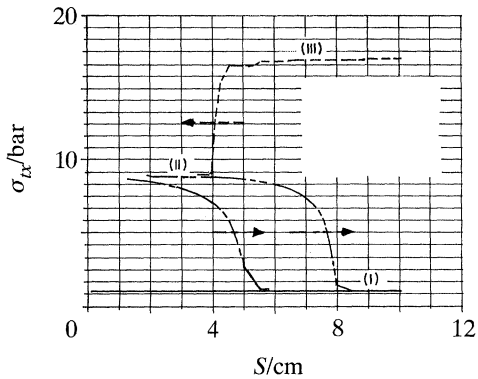

Figure 27. The rubber stress against distance for various times. ——, $t = 2.93$ ms; – – –, $t = 3.73$ ms; – – – –, $t = 4.13$ ms; – –, $t = 5.33$ ms.

a longer time interval has to be covered. This is the case in figure 26*b*, where the time difference between successive frames is 400 μs. The displacement of the rubber supported plate, and the rubber rod deformation, is clearly visible in this figure. Substituting the initial conditions of the considered experiment ($M_s = 1.562$, $A_g = 0.0032$ m^2, $w_d = 31.76$ g) in (59) yields that the transmitted shock wave should be formed at a distance of about 5.8 cm, measured from the initial position of the rubber-rod leading edge.

PHILOSOPHICAL TRANSACTIONS OF THE ROYAL SOCIETY A MATHEMATICAL, PHYSICAL & ENGINEERING SCIENCES

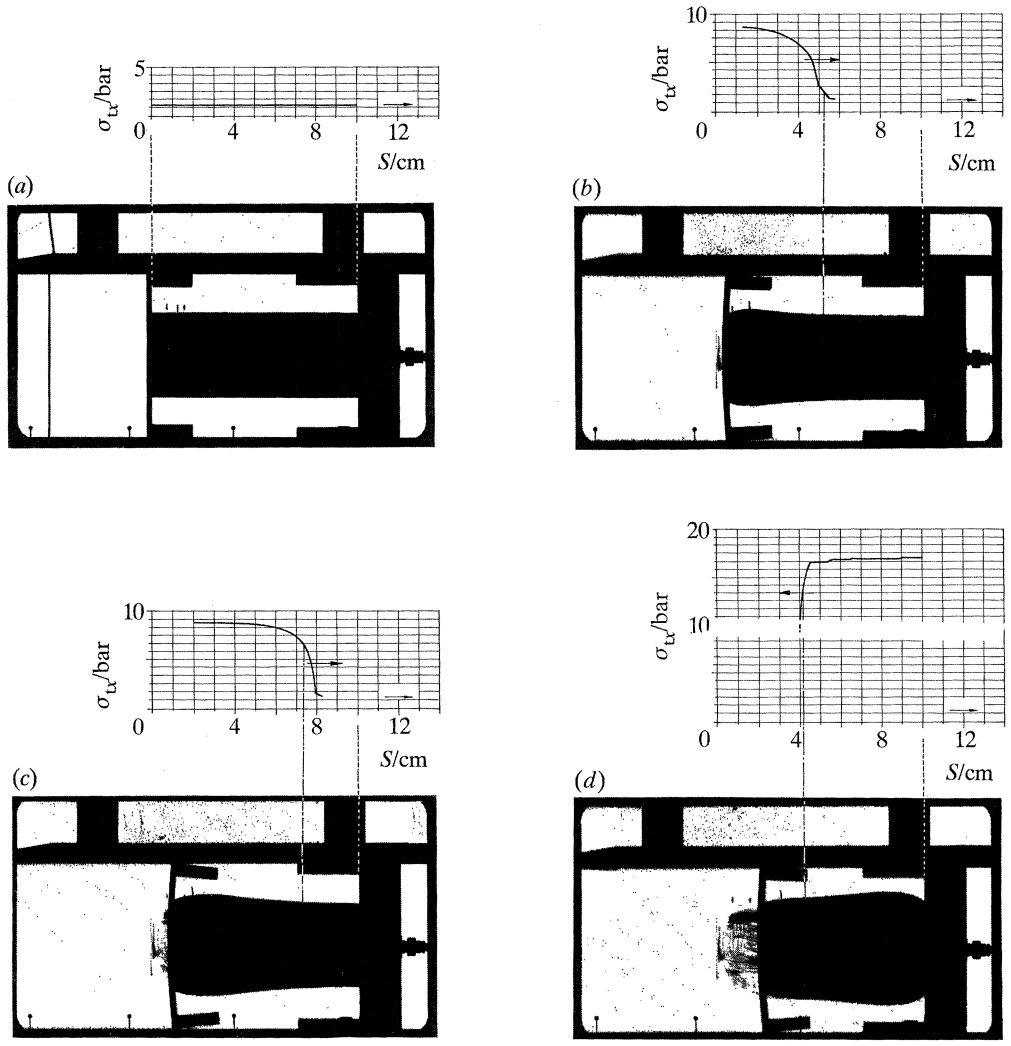

Figure 28. Single shadowgraphs showing specific events from the incident shock wave collision with the rubber-supported plate (frames 1, 3, 4, and 7 of figure 26*b*). (*a*) Frame 1, $t = 2.93$ ms; (*b*) frame 3, $t = 3.73$ ms; (*c*) frame 4, $t = 4.13$ ms; (*d*) frame 7, $t = 5.33$ ms.

In figure 27 numerical results obtained for the rubber stress, at four different times: $t = 2.93$ ms (which corresponds to the event shown in frame 1 of figure 26*b*; i.e. before collision), 3.73 ms (which corresponds to frame 3 of figure 26*b*), 4.13 ms (which corresponds to frame 4, in figure 26*b*) and 5.33 ms (which corresponds to frame 7 in figure 26*b*) are shown. It is apparent that at $t = 3.73$ ms the transmitted compression wave head is located at $S \approx 5.3$ cm. This is verified in figure 28*b* where a change in the rubber's width is evident at $S \approx 5$ cm. The position along the x-axis where changes in the width of the rubber rod are first noticed is most likely the location of the head of the compression wave. For $t = 4.13$ ms it is clear from figure 27 that the compression wave coalesces to a shock wave whose position is at $S \approx 7.5$ cm. (Now the changes in the rubber width are larger than those shown in frame 3, figure 28*b*; this confirms the existence of a shock wave in frame no. 4.) It

Figure 29

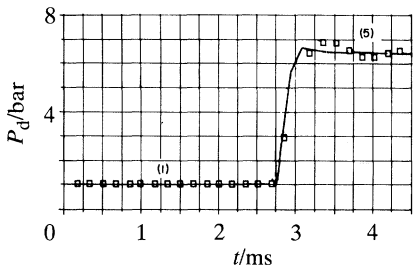

Figure 30

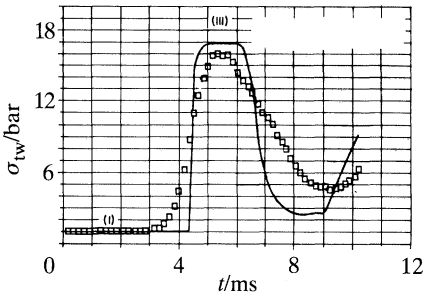

Figure 29. Pressure history on the rubber supported plate; ——, numerical results; □, experimental findings.

Figure 30. Stress at the rubber rear-end where it is attached to a rigid wall; ——, numerical results; □, experimental findings.

is apparent from figure 28*c* that the shock wave position is roughly at $S \approx 7.5$ cm. At $t = 5.33$ a reflected shock wave propagates in the rubber (figure 27); for this time figure 28*d* indicates the existence of the reflected shock wave. It is evident from figure 28*b*, *c* that there is a fairly good agreement between the numerically predicted position of the shock wave and the experimental findings.

A comparison between the numerical and experimental results for the pressure acting on the rubber-supported plate is available in figure 29. The experimental points were deduced from figure 24; the pressure variations are terminated at $t \approx 4.5$ ms (about 1.5 ms after the head-on collision) since at later times the recorded pressure includes the wave interactions which, as mentioned earlier, are not included in the present physical model. Good agreement between the two results is evident from figure 29.

Experimental and numerical results obtained for the rubber stress at its rear end, where it is attached to a rigid wall, are given in figure 30. Fair agreement is witnesed for the early part of the rubber compression process. The agreement deteriorates at a later time due to friction between the rubber rod and the shock tube windows and the pressure increase on the plate due to the interaction between the reflected shock wave and the contact surface. Both of these effects are not included in the numerical solution. Comparing the results shown in figure 30 with those of figure 23 indicates that the raise in the rubber stress is much quicker in the former and that it reaches a constant value for a short time. This is a further indication that a shock wave is reflected from the rear-end of the rubber rod.

5. Summary and conclusions

A physical model for describing the head-on collision process between a normal shock wave and a rubber supported plate was developed. This model was solved numerically for three different modes of rubber loading. The numerical solution provides information regarding the gas flow and the rubber properties at different times and locations. It was found that the speed of the wave propagation, in the rubber, for the case of uni-axial strain loading is much larger than that obtained for uni- and bi-axial stress loading cases. At an early time after the head-on collision higher pressure behind the reflected shock wave was obtained in the case of uni-axial

PHILOSOPHICAL TRANSACTIONS OF THE ROYAL SOCIETY A MATHEMATICAL, PHYSICAL & ENGINEERING SCIENCES

strain loading, as compared with the other two loading cases. However, in all three loading modes the pressures obtained behind the reflected shock wave were lower than that obtained in a similar reflection from a rigid wall. At a later time after the collision, due to the transmitted shock wave, the pressure acting on the rubber-supported plate was higher than that obtained in a similar reflection from a rigid wall. Furthermore, now the highest pressure (P_6) is obtained in the uni-axial stress loading case while the lowest corresponds to the uni-axial strain loading case. The stresses in the rubber leading edge ($\sigma_{t,d}$) and in its rear end ($\sigma_{t,w}$) were significantly higher than the pressure acting on the rubber supported plate (P_5) and/or the pressure behind a reflected shock wave in a similar rigid wall case. It should be noted here that both $\sigma_{t,d}$ and $\sigma_{t,w}$ are strongly affected by the area ratio A_g/A_r. The obtained results should be used only for the specified area ratios. In the examples solved the highest rubber stress, and the smallest strain, were obtained in the uni-axial strain loading while the lowest stress, and the highest strain, were found in the uni-axial stress loading case.

The case of bi-axial stress loading was investigated both numerically and experimentally. Good agreement was obtained between the experimental and numerical results for the plate displacement, the pressure behind the reflected shock wave, and the stress at the rubber-rod rear-end. This agreement confirms the validity of the proposed model and the reliability of the numerical scheme used for its solution.

When presenting the numerical results for the rubber variables as a function of distance, for different times, the existence of the wave patterns, shown schematically in figure 4 was confirmed. Repeating this computational procedure for the gaseous phase would confirm the expected wave patterns in this phase (see Mazor 1989). It was also shown that by proper selection of the physical properties of the rubber and the plate it supports one could ensure that the transmitted compression wave in the rubber rod will either remain a compression wave or coalesce into a shock wave.

This research was supported by a grant from the German–Israeli Foundation for Scientific Research and Development. Their support is acknowledged with thanks. The typescript of the present paper was prepared while one of the authors (O.I.) was a visiting professor at the Shock Wave Research Center of the Tohoku University in Sendai, Japan. This stay made possible the requisite concentration and clear thought by virtue of which the completion of this work was made possible. The author is thankful for this opportunity.

References

Alpher, R. A. & Rubin, R. J. 1954 *J. appl. Phys.* **25**, 394–395.

Beavers, G. S. & Matta, R. K. 1972 *AIAA J.* **10**, 959–961.

Boris, J. P. & Book, D. L. 1973 *J. compt. Phys.* **11**, 38–69.

Borisov, A. A., Gelfand, B. E., Kudinov, V. M., Palamorchuk, B. I., Stephanov, V. V., Timofeev, A. I. & Chomic, S. V. 1978 *Acta Astronautica* **5**, 1027–1033.

Boyer, D. W., Brode, H. L., Glass, I. I. & Hall, J. C. 1958 University of Toronto, Institute for Aerospace Studies, UTIAS Rep. no. 48.

Boyer, D. W. 1959 University of Toronto, Institute for Aerospace Studies, UTIAS Rep. no. 58.

Brode, H. L. 1955 *J. appl. Phys.* **26**, 766–775.

Brode, H. L. 1959 *Phys. Fluids* **2**, 217–229.

Clarke, J. F. 1984 *Q. Jl Mech. appl. Math.* **37**, 87–111.

Courant, R. & Friedrichs, K. O. 1948 *Supersonic flow and shock waves*. New York: Interscience Publications.

Gelfand, B. E., Gubin, S. A., Kogarko, S. M. & Popov, O. E. 1975 *J. appl. Mech. Tech. Phys.* **6**, 897–900. (English translation.)

Gelfand, B. E., Gubanov, A. V. & Timofeev, A. I. 1983 *Fluid Dynam.* **18**, 561–566.

Gelfand, B. E., Gubanov, A. V. & Timofeev, A. I. 1984 *Izv. Akad. Nauk SSSR Mekh. Zhidk. Gaza* no. 4, 85–92.

Glass, I. I. & Hall, J. G. 1959 Shock tubes. In *Handbook of supersonic airodynamics*, §18 (ed. S. L. Penn) NAVORD Rep. 1488 (vol. 6). Bureau of Naval Weapon Publication.

Glimm, J. 1965 *Communs pure appl. Math.* **18**, 697–715.

Godunov, S. K. 1959 *Math. Sb.* **47**, 357–393.

Gvozdeva, L. G., Faresov, Y. M., Brossard, J. & Charpentier, N. 1986 In *Dynamics of explosions* (ed. J. R. Bowen, J. C. Leyer & R. I. Soloukhin), pp. 155–165, Progress in Aeronautics and Astronautics, vol. 106. New York.

Harding, J. 1976 *Sci. Prog. Oxf.* **63**, 575–603.

Mazor, G., Ben-Dor, G., Mond, M. & Igra, O. 1988 *AIAA J.* **26**, 116–119.

Mazor, G. 1989 The influence of surface properties on the head-on reflection of shock waves. Ph.D. thesis, Ben-Gurion University of the Negev, Beer Sheva, Israel. (In Hebrew.)

Meyer, R. F. 1957 *J. Fluid Mech.* **3**, 309–323.

Monti, R. 1970 *Mechanica J. Ital. Ass. Theo appl. Mech.* **5**, 285–296.

Muirhead, J. C. 1958 Canadian Defense Research Establishment Suffield DRES TN-142.

Nowinski, J. L. 1965 *J. Eng. Industry* **87**, 523–529.

Pack, D. C. 1957 *Phil. Mag.* **2**, 182–195.

Rakib, Z., Mond, M., Ben-Dor, G. & Igra, O. 1989 *J. Plasma Phys.* **41**, 355–380.

Rivlin, R. S. 1948 *Phil. Trans. R. Soc. Lond.* A **240**, 459–525.

Treloar, L. R. G. 1958 *The physics of rubber elasticity*. Oxford: Clarendon Press.

Treloar, L. R. G. 1974 In *Rubber and rubber elasticity* (ed. A. S. Dunn), pp. 107–123. New York and London: Wiley.

Valanis, K. C. & Landel, R. F. 1967 *J. appl. Phys.* **38**, 2997–3002.

von-Neumann, J. & Richtmeyer, R. D. 1950 *J. appl. Phys.* **21**, 232–233.

Wienfield, F. H. & Hill, D. A. 1977 Canadian Defence Research Establishment, Suffield, Rep. DRES TN-389.

Wlodarczyk, E. 1980 *J. Tech. Phys.* **21**, 505–515.

Wlodarczyk, E. 1981 *J. Tech. Phys.* **22**, 201–215.

Received 19 November 1990; revised 14 March 1991; accepted 16 April 1991

PHILOSOPHICAL TRANSACTIONS OF THE ROYAL SOCIETY A MATHEMATICAL, PHYSICAL & ENGINEERING SCIENCES

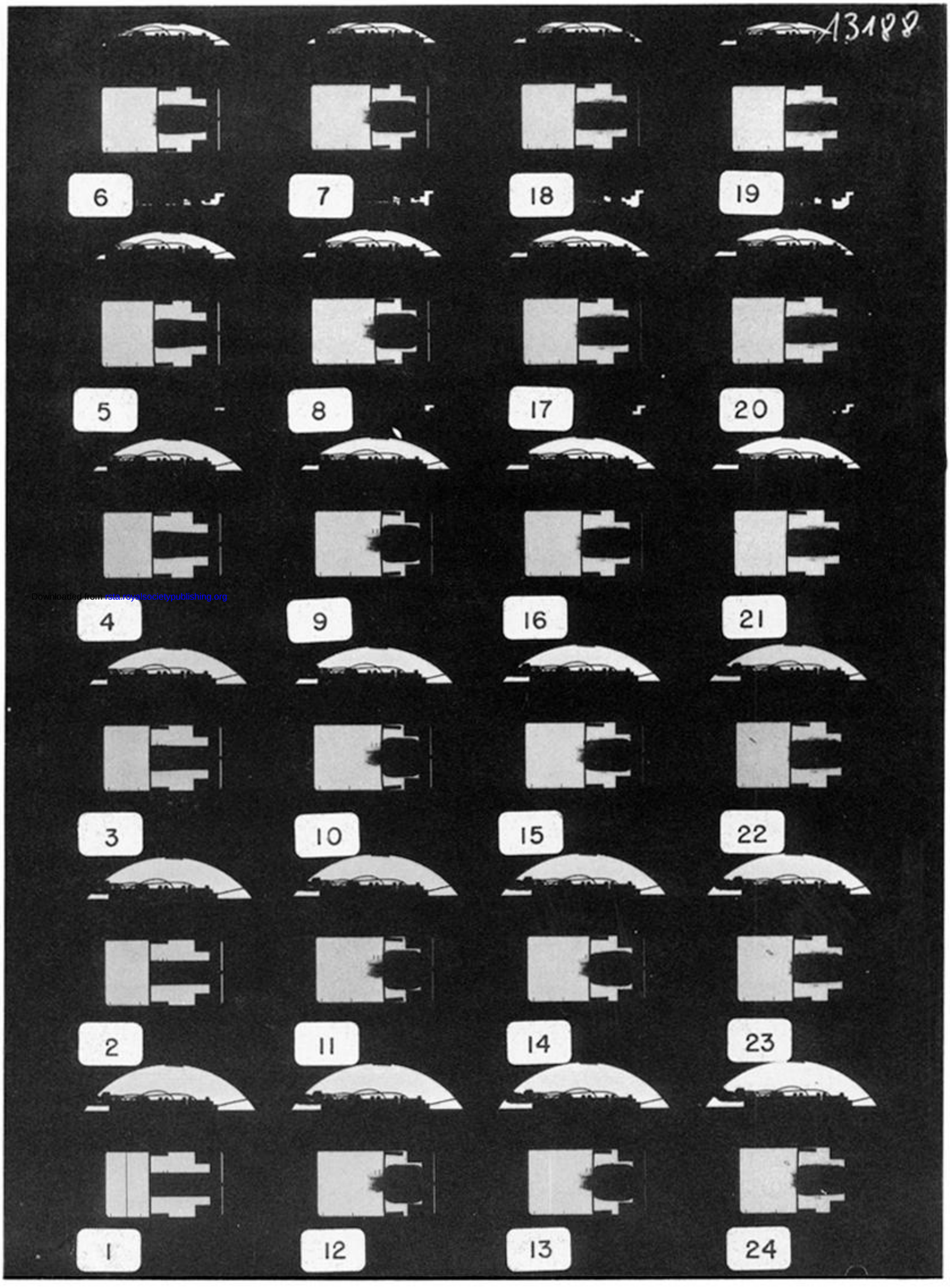

Figure 19. Shadowgraphs during and after the head-on collision between the incident shock wave and the rubber supported plate: The time elapsed between successive frames is 400 μs.

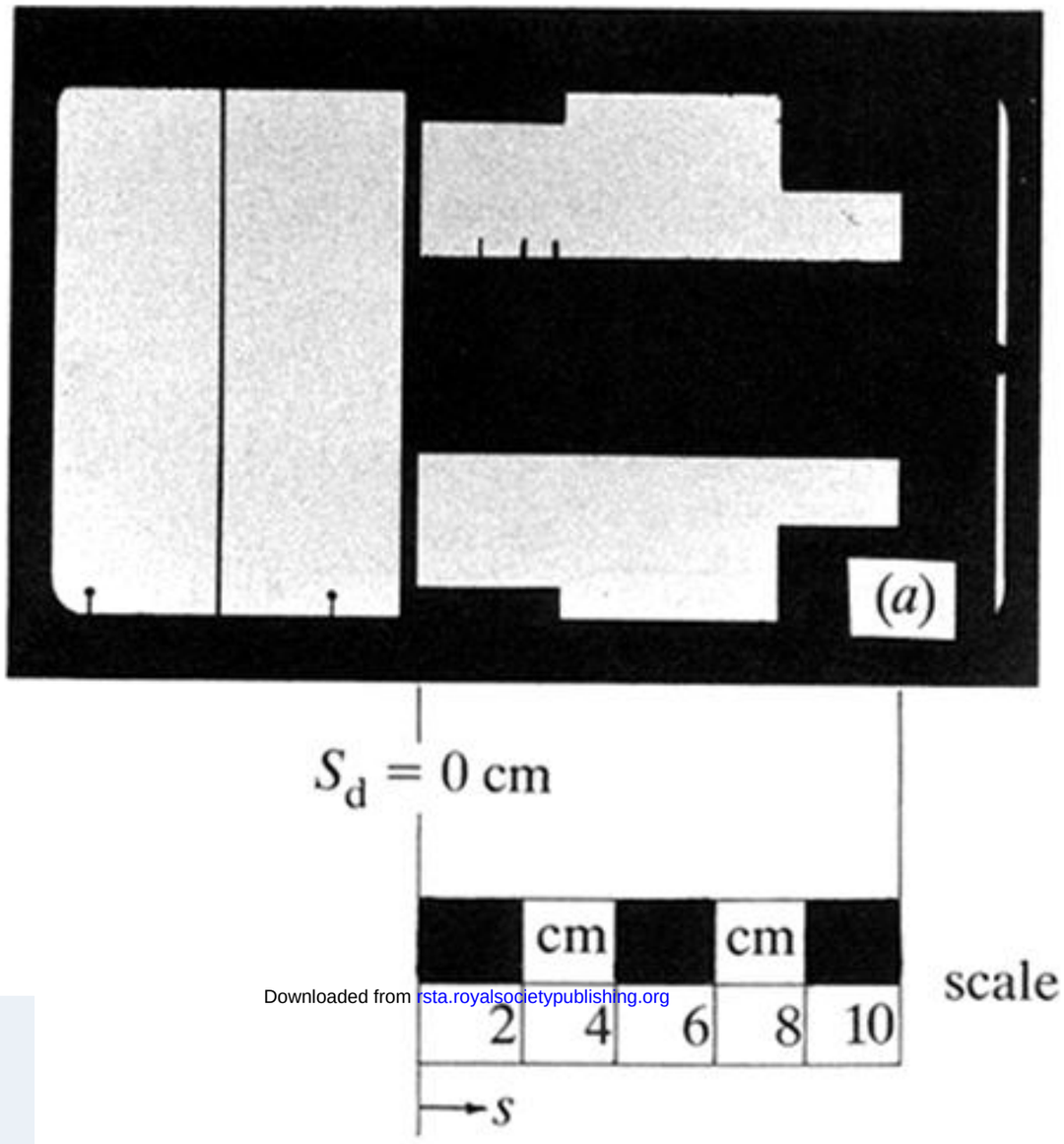

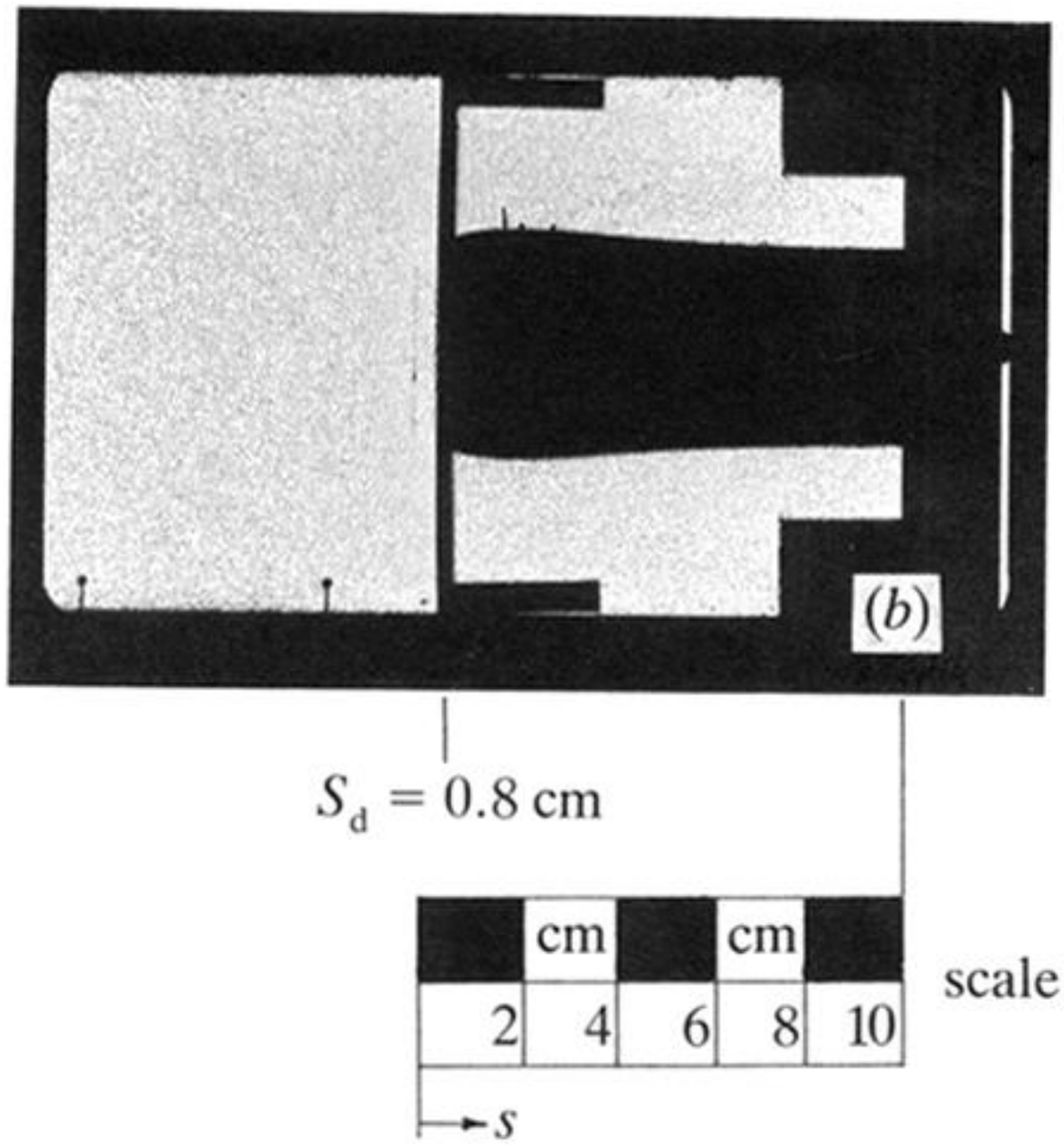

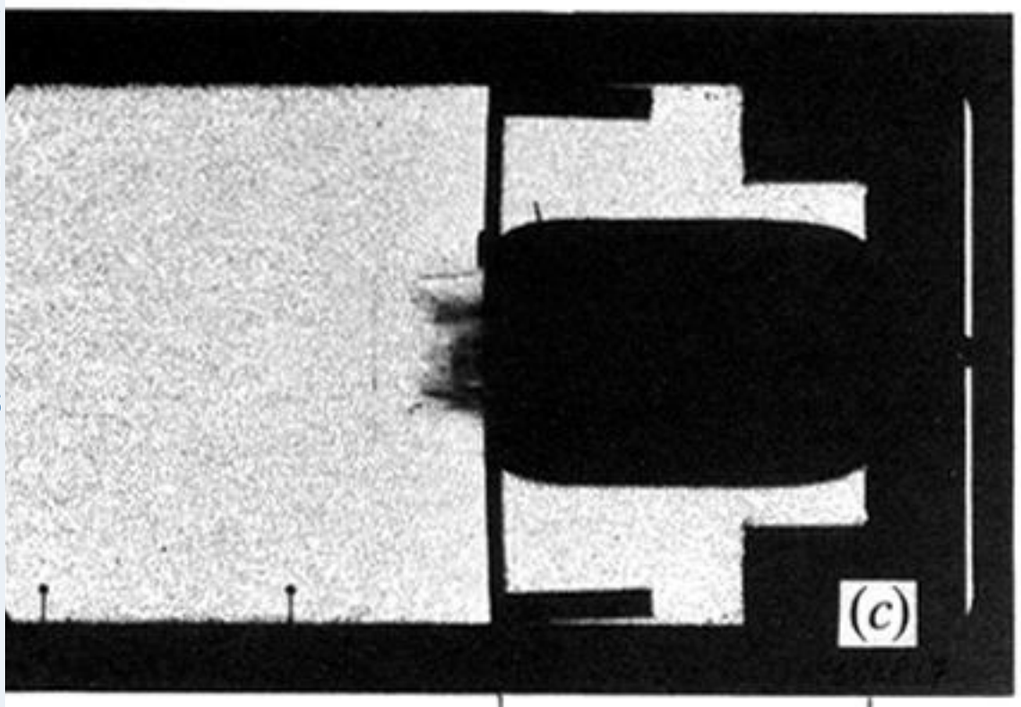

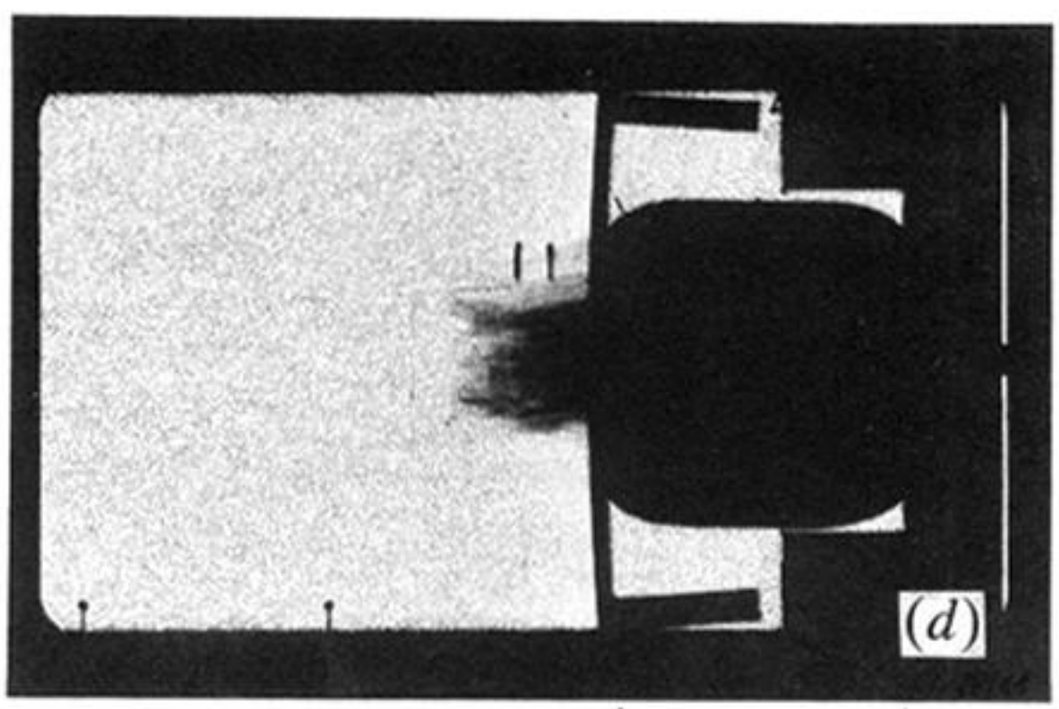

Figure 20. Enlargement of shadowgraphs of figure 19: (*a*) frame no. 1, $t = 2.78$ ms; (*b*) frame no. 4, $t = 4$ ms; (*c*) frame no. 7, $t = 5.2$ ms; (*d*) frame no. 11, $t = 6.8$ ms.

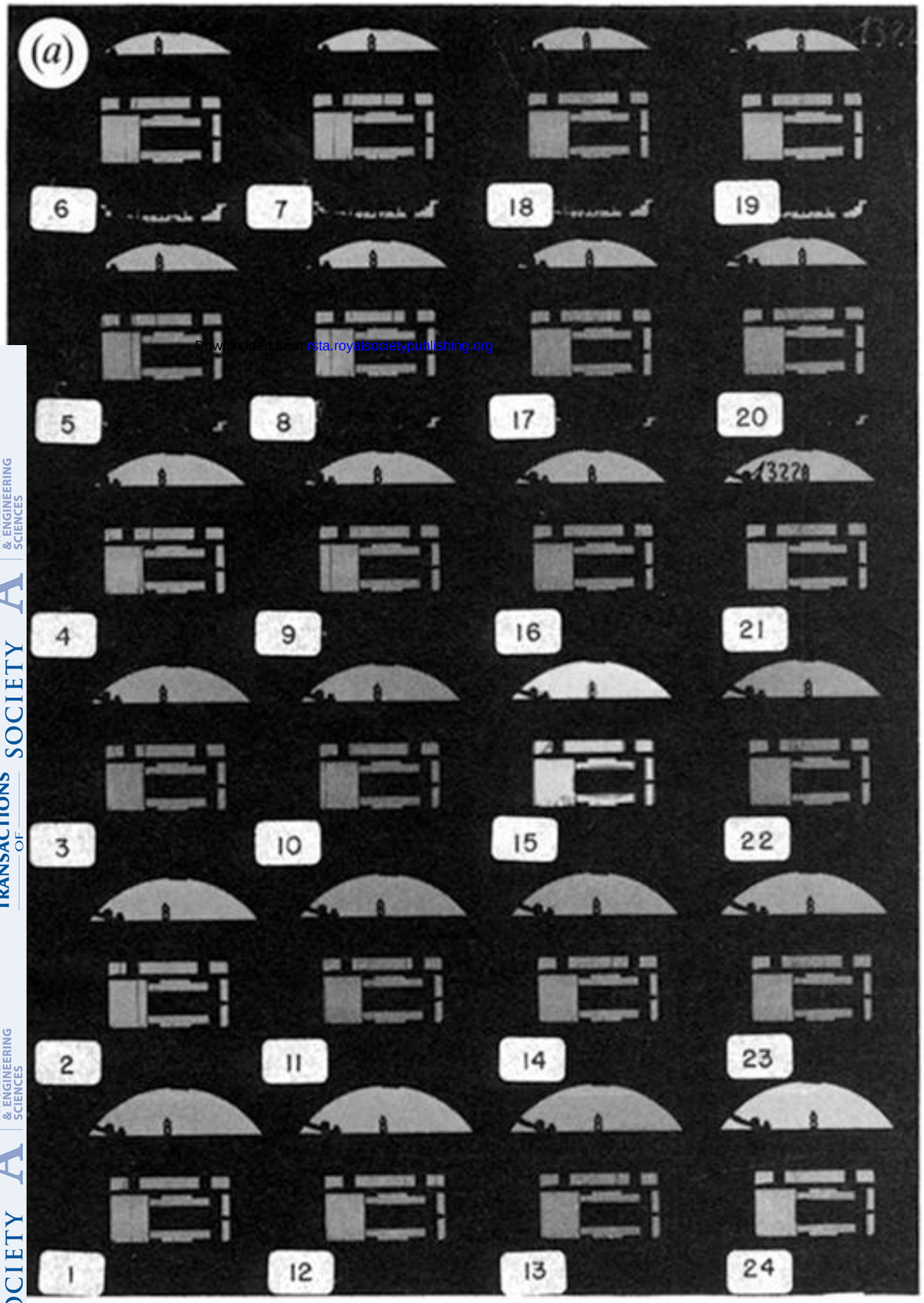

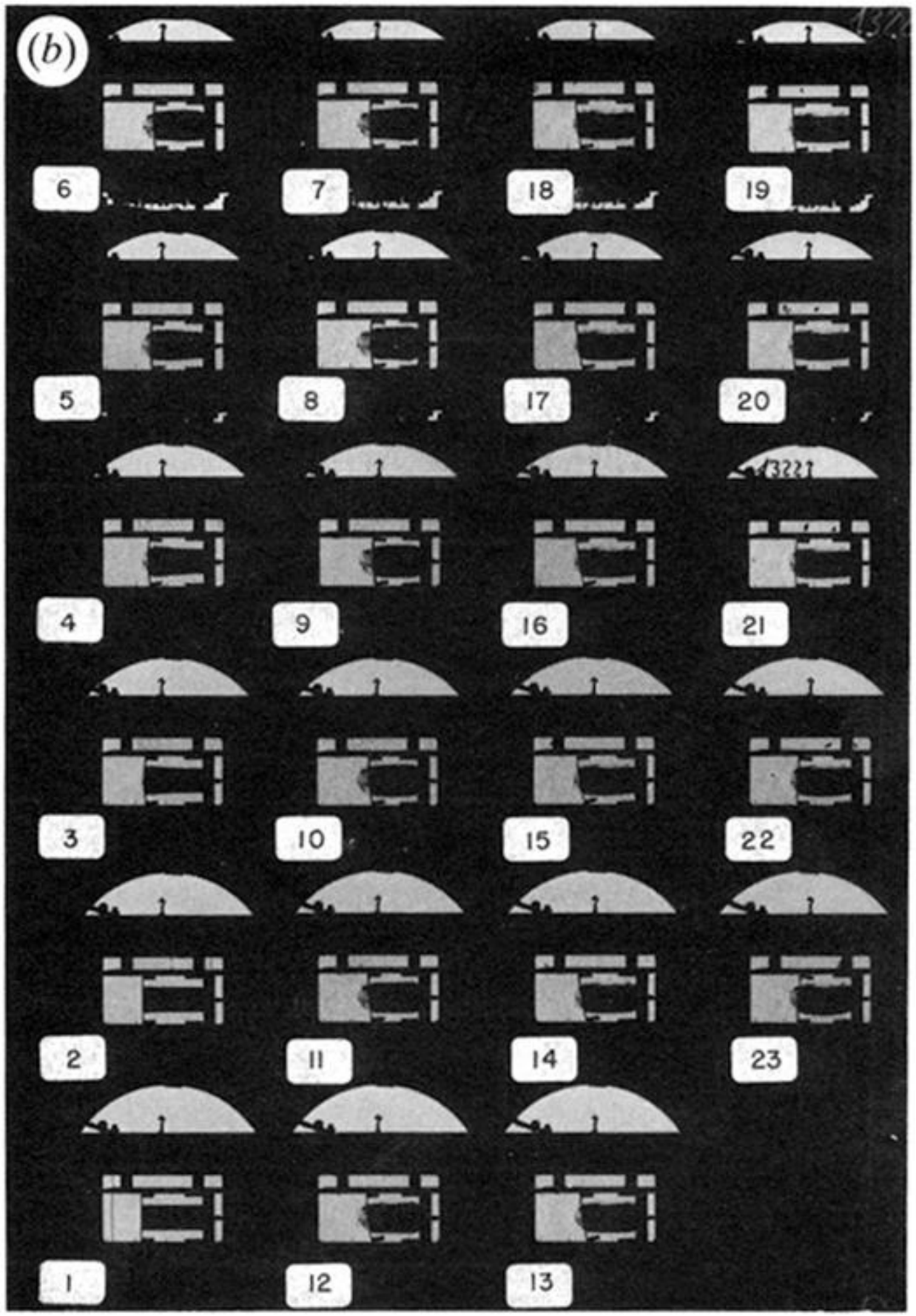

Figure 26. (*a*) Shadowgraphs during and after the head-on collision between the incident shock wave and the rubber-supported plate. The time elapsed between successive frames is 25 μs. (*b*) Shadowgraphs during and after the head-on collision between the incident shock wave and the rubber-supported plate. The time elapsed between successive frames is 400 μs.

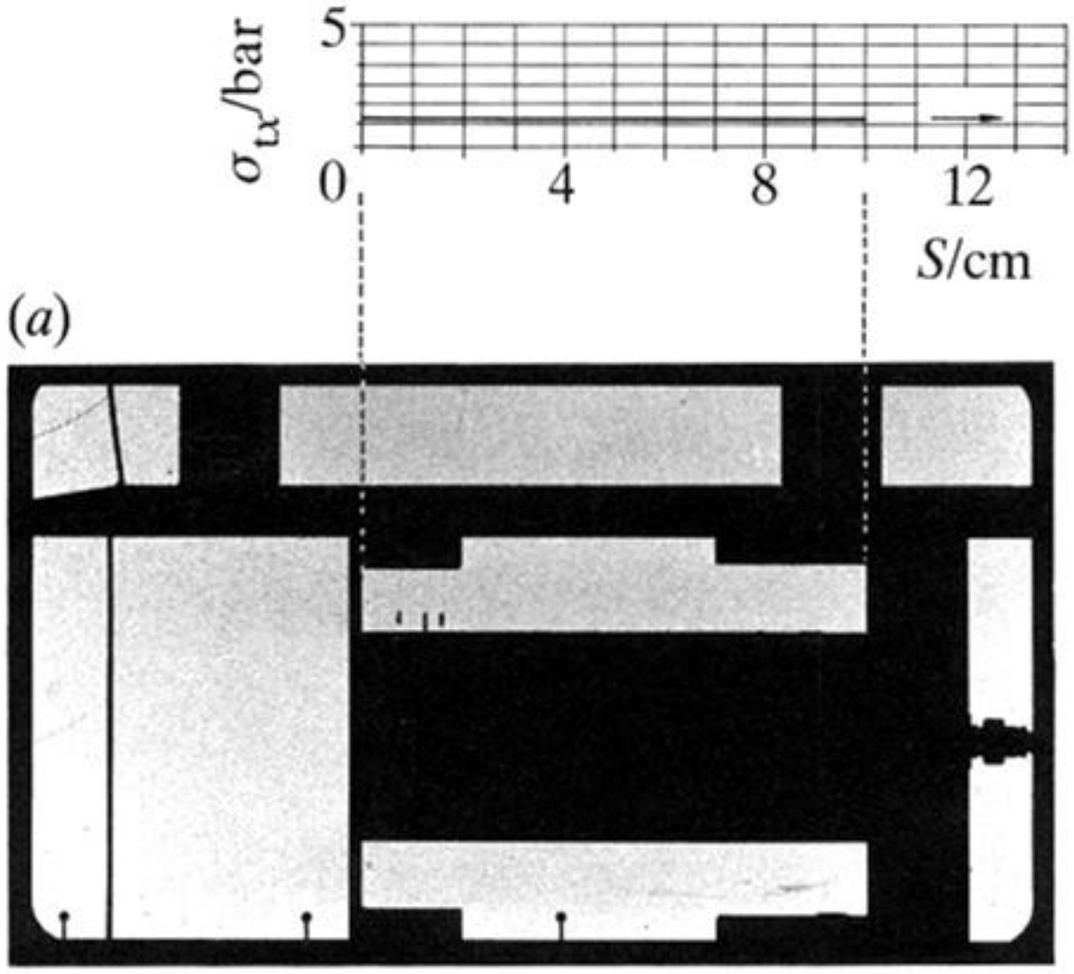

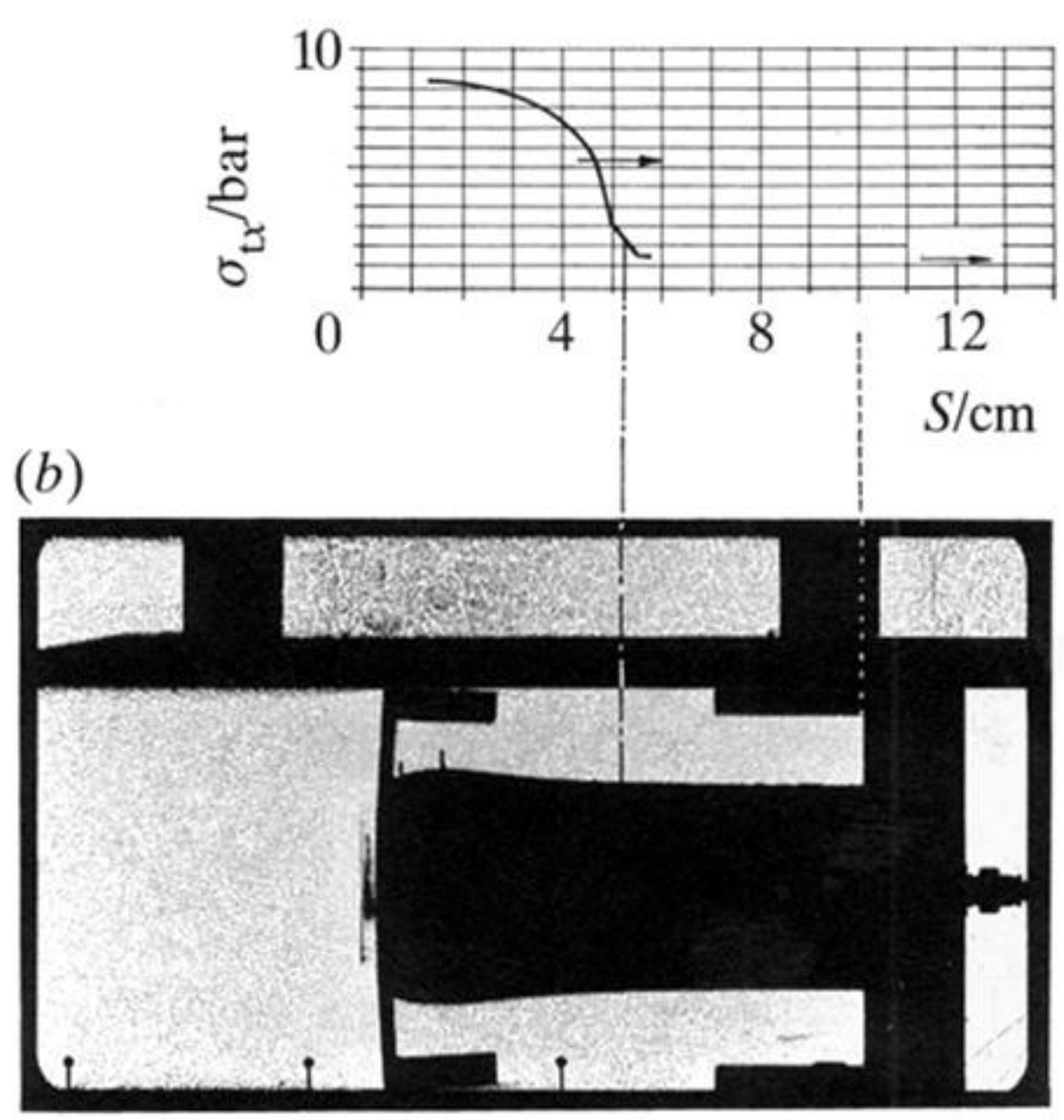

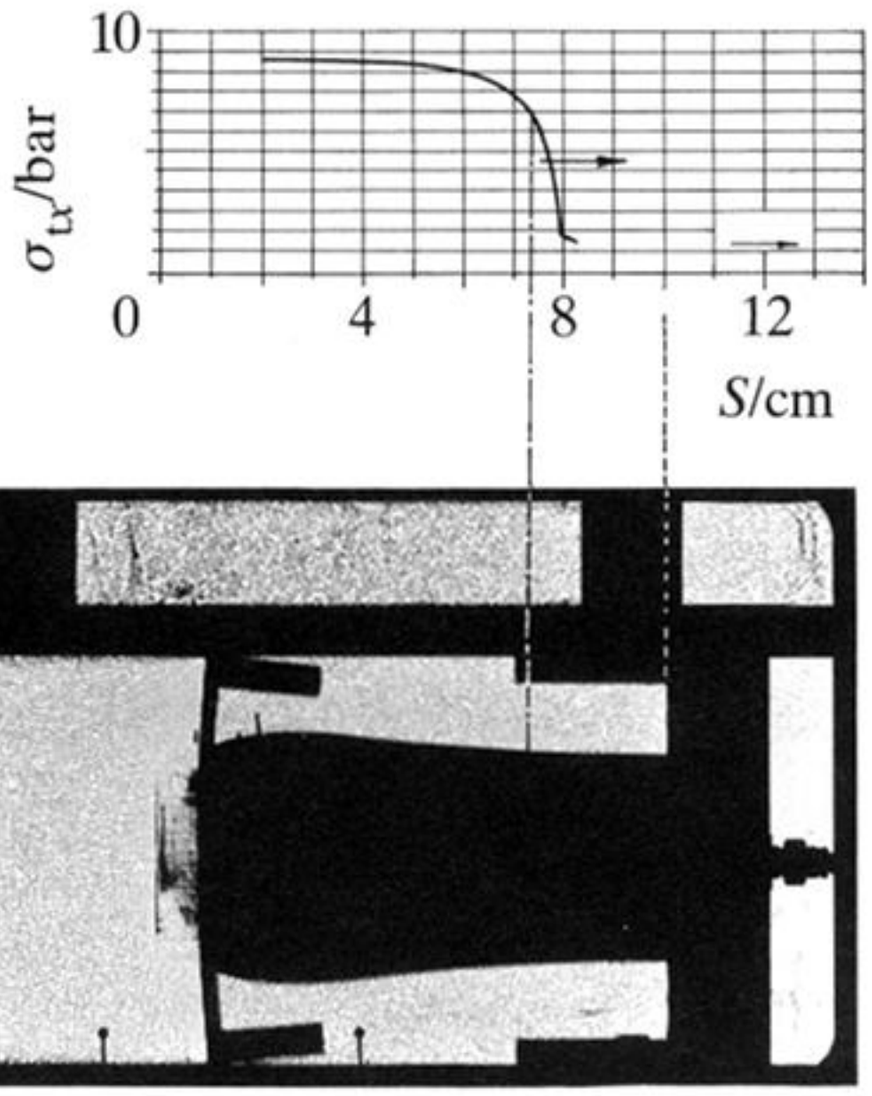

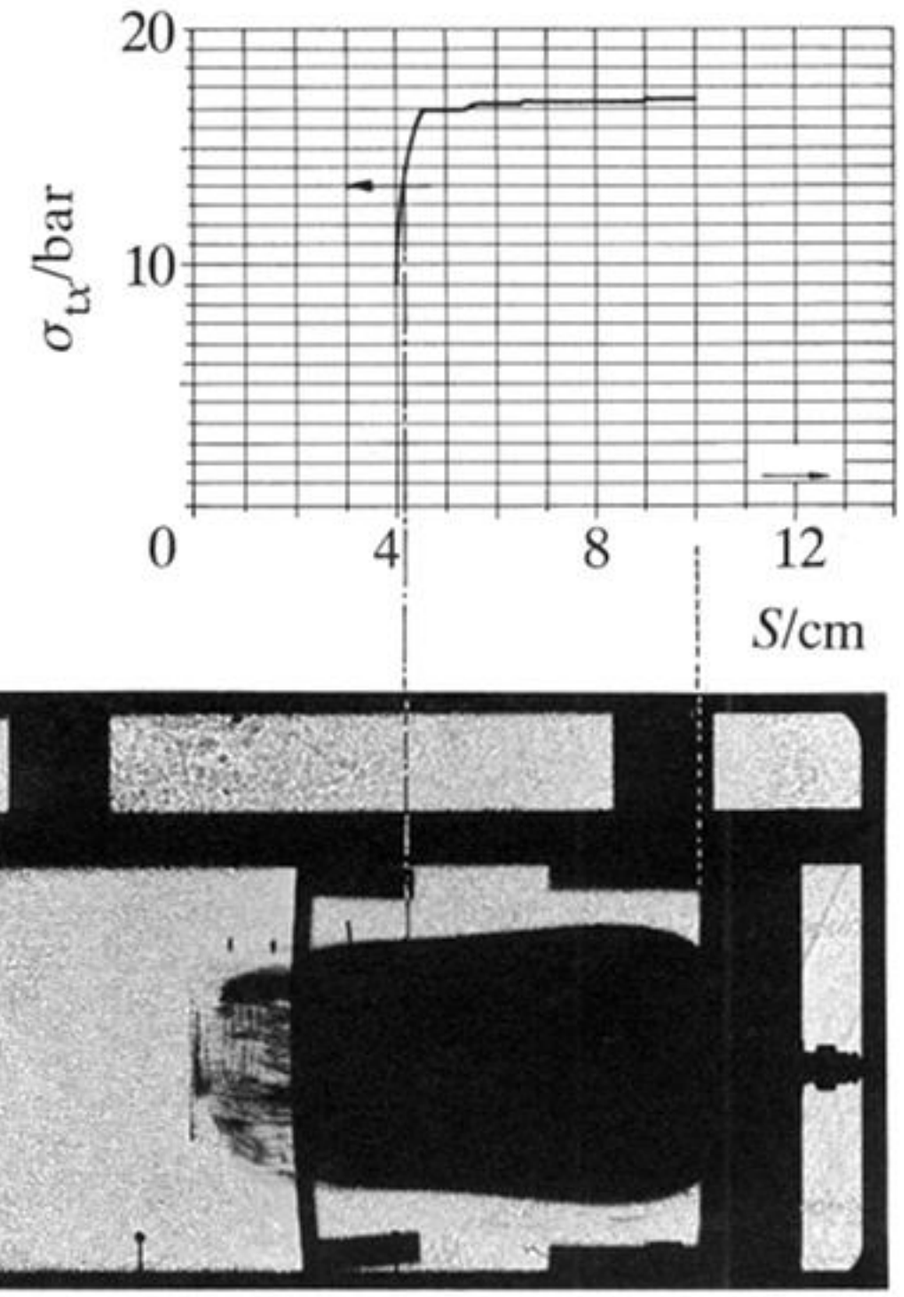

Figure 28. Single shadowgraphs showing specific events from the incident shock wave collision with the rubber-supported plate (frames 1, 3, 4, and 7 of figure 26*b*). (*a*) Frame 1, $t = 2.93$ ms; (*b*) frame , $t = 3.73$ ms; (*c*) frame 4, $t = 4.13$ ms; (*d*) frame 7, $t = 5.33$ ms.